Remote Sensing of Environment 295 (2023) 113699

Contents lists available at ScienceDirect

Remote Sensing of Environment

journal homepage: www.elsevier.com/locate/rse

Generating high-resolution total canopy SIF emission from TROPOMI data: Algorithm and application

Zhaoying Zhang [a,b,d,*], Yao Zhang [c], Yongguang Zhang [a,b,d]

[a] International Institute for Earth System Sciences, Jiangsu Center for Collaborative Innovation in Geographical Information Resource Development and Application, Nanjing University, Nanjing, Jiangsu, China

[b] Jiangsu Provincial Key Laboratory of Geographic Information Science and Technology, Key Laboratory for Land Satellite Remote Sensing Applications of Ministry of Natural Resources, School of Geography and Ocean Science, Nanjing University, Nanjing, Jiangsu 210023, China

[c] College of Urban and Environmental Sciences, Peking University, Beijing, China

[d] International Joint Carbon Neutrality Laboratory, Nanjing University, Nanjing, Jiangsu 210023, China

A R T I C L E I N F O

Edited by Jing M. Chen

Keywords:
SIF
GPP
High spatial resolution
Footprint
Spatial mismatch

A B S T R A C T

Solar-induced chlorophyll fluorescence (SIF) is a rapidly advancing front in modeling global terrestrial gross primary production (GPP). Canopy total SIF emissions (SIF_{total}) are mechanistically linked to the plant photosynthesis, and can be estimated from satellite observed SIF (SIF_{obs}) through radiative transfer modeling. However, the current satellite SIF_{obs} and thus SIF_{total} are available only at coarse spatial resolutions from several kilometers to tens of kilometers, inhibiting the application at fine spatial scales. Here, we proposed an algorithm to generate both global high-resolution SIF_{total} ($HSIF_{total}$) and high-resolution SIF_{obs} ($HSIF_{obs}$) at 1 km from low-resolution SIF_{obs} ($LSIF_{obs}$) from the TROPOspheric Monitoring Instrument (TROPOMI), which has a spatial resolution at nadir of 3.5 km by 5.6–7 km. Our statistical method is based on the law of energy conservation and uses satellite derived fraction of absorbed photosynthetically active radiation, fluorescence efficiency, and the escape probability of fluorescence. We evaluated the accuracy of our $HSIF_{total}$ using the Orbiting Carbon Observatory-2 SIF ($R^2 = 0.78$). We found that the spatial resolution had clear effects on the relationship between $HSIF_{total}$ and GPP. We also compared $HSIF_{total}$ to 8-day averaged tower GPP from 135 flux sites and found that they were better correlated when $HSIF_{total}$ was averaged over a 1-km radius around the tower than when averaged over a larger radius. Our study provided a unique high-resolution $HSIF_{total}$ product, which will advance the estimation of GPP by extrapolating site-level relationships to the global scale.

1. Introduction

Satellite solar-induced chlorophyll fluorescence (SIF) can be a proxy of terrestrial gross primary productivity (GPP) from regional to global scales at coarser spatiotemporal scales (Frankenberg et al., 2011; Joiner et al., 2011; Guanter et al., 2012; Doughty et al., 2019; Magney et al., 2020; Porcar-Castell et al., 2021). In recent decades, SIF has been successfully retrieved from multiple satellite sensors, including the Greenhouse Gases Observing SATellite (GOSAT) (Frankenberg et al., 2011), Global Ozone Monitoring Experiment-2 (GOME-2) (Joiner et al., 2011), Orbiting Carbon Observatory-2 (OCO-2) (Sun et al., 2018), TROPOspheric Monitoring Instrument (TROPOMI) (Köhler et al., 2018; Köhler et al., 2020), the Chinese Carbon Dioxide Observation Satellite Mission (TanSat) (Du et al., 2018), and Orbiting Carbon Observatory-3 (OCO-3) (Taylor et al., 2020; Doughty et al., 2022). These platforms have opened new avenues for mapping SIF and modeling GPP globally.

Satellite SIF has been used to estimate GPP using linear SIF-GPP relationship at the site scale, which is commonly calibrated with satellite SIF and flux tower GPP (Li and Xiao, 2019b; Zhang et al., 2020a). However, satellite SIF retrievals usually have coarse footprints (e.g., GOME-2 is 40 km and GOSAT is 10.5 km diameter), which are substantially larger than eddy flux tower footprint (~0.3 km to 1 km depending on site characteristics and environmental conditions) (Chu et al., 2021). Although OCO-2/3 SIF provides a finer footprint (1.3 km × 2.25 km) that is more comparable to the eddy covariance (EC) tower footprint, spatial aggregation is needed to reduce the uncertainty of single SIF retrievals before it can be compared with the EC measurements (Sun et al., 2018; Yu et al., 2019; Doughty et al., 2022).

* Corresponding author at: International Institute for Earth System Sciences, Jiangsu Center for Collaborative Innovation in Geographical Information Resource Development and Application, Nanjing University, Nanjing, Jiangsu, China.

E-mail address: zhaoying_zhang@nju.edu.cn (Z. Zhang).

https://doi.org/10.1016/j.rse.2023.113699
Received 28 April 2022; Received in revised form 5 June 2023; Accepted 21 June 2023
Available online 28 June 2023

When building SIF-GPP relationships, researchers have tried multiple radii that ranged from 2 km to 225 km around the flux sites (Verma et al., 2017; Wood et al., 2017; Li et al., 2018). This approach is feasible for flux sites with large footprints and/or with homogeneous vegetation cover. However, most EC flux measurements are representative of only a relatively small area with a footprint of approximately 0.5 km - 1 km (Duveiller and Cescatti, 2016), and Chu et al. (2021) reported that only a few eddy-covariance sites are in a truly homogeneous landscape. Therefore, the spatial mismatch between eddy tower GPP and satellite SIF could lead to biases in SIF-GPP relationships, which propagate into the GPP estimates.

The mismatch issue could be partially addressed by using downscaled SIF products with higher spatial resolutions, such as SIF* (Duveiller and Cescatti, 2016; Duveiller et al., 2020), CSIF (Zhang et al., 2018a), RSIF (Gentine and Alemohammad, 2018), GOSIF (Li and Xiao, 2019a), SIF_{oco2_005} (Yu et al., 2019), SIF_{005} (Wen et al., 2020), DSIF (Ma et al., 2022), SDSIF (Hu et al., 2022), and SIF_{net} (Gensheimer et al., 2022), most of which predict SIF at finer spatial resolution using Moderate Resolution Imaging Spectroradiometer (MODIS) surface reflectance, auxiliary data, and empirical or semiempirical statistical models. However, except for SIF_{net}, these products are generated at a spatial resolution of 0.05°, which is still much larger than EC footprints. In addition, these products may miss information of fluorescence efficiency (i.e., the fraction of absorbed radiation photons that are reemitted as SIF photons). The to-be-launched Fluorescence Explorer (FLEX) satellite from the European Space Agency will provide SIF at ~300 m spatial resolution (Drusch et al., 2016), which is comparable to the footprint of flux sites, but it will have a long revisit cycle of 27 days.

The varying escape probability of SIF from different canopy structures (Liu et al., 2020; Zhang et al., 2020a) and sun-target-view geometries (Zhang et al., 2018b; Zhang et al., 2020b) also affect retrieved SIF values and hinders the accurate estimation of GPP using SIF observed by sensors (SIF_{obs}). For this reason, several researchers have proposed estimating the total canopy SIF emission (SIF_{total}) at the leaf level (Zeng et al., 2019; Zhang et al., 2019; Zhang et al., 2020a) or photosystem level (Liu et al., 2019; Liu et al., 2020; Zhang et al., 2021) to reduce the angular and canopy structural effects on SIF_{obs}. Many researchers have reported that SIF_{total} showed better relationships with GPP than SIF_{obs} (Zhang et al., 2019; Lu et al., 2020; Liu et al., 2022). Moreover, after mitigating the effects of the escape probability on SIF_{obs} by calculating SIF_{total}, it is possible to establish a nearly universal model for SIF_{total} and GPP across biomes, at least for C_3 plants (Zhang et al., 2020a).

Since the high-resolution (such as 1 km) satellite SIF_{total} ($HSIF_{total}$) is not currently available, a new algorithm is needed to downscale the current low-resolution satellite SIF_{obs} ($LSIF_{obs}$) to $HSIF_{total}$. Once $HSIF_{total}$ is estimated, the effects of spatial mismatch in the footprint between SIF and GPP can be investigated by comparing in situ GPP and $HSIF_{total}$ averaged from different radii around the flux site and then analyzing the effects of the search radius (or spatial mismatch in footprint) on the relationship between GPP and $HSIF_{total}$. Therefore, the main objective of this study was to fill the knowledge gap in understanding the SIF-GPP relationship by mitigating the effects due to spatial mismatch, canopy structure, and directionality of SIF.

2. Materials and methods

2.1. TROPOMI and OCO-2 SIF data

Two spaceborne (TROPOMI and OCO-2) SIF products were used in this study. TROPOMI is an imaging spectrometer onboard the Sentinel-5 Precursor satellite launched on 13 October 2017, co-funded by ESA and the Netherlands. TROPOMI provides spectral measurements with a swath of approximately 2600 km and a spatial resolution at nadir of 3.5 km × 7 km before August 6th, 2019, and 5.6 km × 3.5 km after August 6th, 2019. TROPOMI SIF is retrieved at the spectral ranges of 735–758 nm and 743–758 nm (Guanter et al., 2021). All SIF products were normalized to 740 nm using a reference fluorescence spectrum. TROPOMI SIF using the spectral range of 743–758 nm was used in this study. The OCO-2 SIF Lite product (v11r) provides a nominal spatial resolution of 1.3 km × 2.25 km (denoted as footprint) at nadir, with eight cross-track footprints together covering a maximum ~10 km-wide full swath (Frankenberg et al., 2014; Sun et al., 2018; Doughty et al., 2022). OCO-2 SIF is originally retrieved at 757 nm and 771 nm, but the OCO-2 SIF products also provide the SIF normalized at 740 nm, which we used. For TROPOMI SIF, observations with cloud fractions <0.2 were used (Zhang et al., 2019). For OCO-2 SIF, observations with quality flags of 0 (best quality) and 1 (good quality) were used.

2.2. Spatial downscaling framework for $HSIF_{total}$

The overall strategy of downscaling area-based SIF is based on the law of energy conservation, describing that the observed SIF at a low spatial resolution ($LSIF_{obs}$) is the arithmetic mean of high-resolution SIF_{obs} for each 0.0083° × 0.0083° (denoted as 1 km × 1 km afterwards) subpixel i ($HSIF^i_{obs}$):

$$LSIF_{obs} = \sum_{i=1}^{n} HSIF^i_{obs} \Big/ n \tag{1}$$

where n is the number of $HSIF_{obs}$ in a footprint of $LSIF_{obs}$. Note that the superscript i represents the 1 km × 1 km subpixel in a single footprint of $LSIF_{obs}$ or a 0.2° grid throughout the manuscript. The application of the law of energy conservation in this way is justified because SIF is energy that reaches the sensor. Using this concept, $LSIF_{obs}$ can be partitioned into several $HSIF_{obs}$ 1 km grid cells. As shown in Fig. 1A, a single TROPOMI $LSIF_{obs}$ footprint covers several 1 km × 1 km subpixels (shown as the smallest boxes). Due to the high atmospheric transmittance in the SIF retrieval window of 743–758 nm (Guanter et al., 2021), the atmospheric effects (including absorption and scattering) under clear-sky conditions was negligible. Therefore, the law of energy conservation is still applicable between top-of-canopy emission and observation at the satellite sensor.

To better explain the downscaling process, we first introduce the light use efficiency model for SIF (Guanter et al., 2014):

$$SIF_{total} = PAR \times FPAR_{chl} \times \Phi_F \tag{2}$$

$$SIF_{obs} = SIF_{total} \times f_{PC} \tag{3}$$

where PAR is the flux of photosynthetically active radiation, $FPAR_{chl}$ is the fraction of incident PAR irradiance absorbed by chlorophyll, Φ_F is the fluorescence efficiency (i.e., the fraction of absorbed PAR photons that are reemitted as SIF photons), and f_{PC} is the escape probability of SIF photons from photosystem to canopy. Based on Eq. (3), the different magnitudes between SIF_{obs} and SIF_{total} were reasonable. Applying the light use efficiency model for SIF to the subpixel, we can obtain:

$$\frac{HSIF^i_{total}}{\sum_{i=1}^{n} HSIF^i_{total} \times f^i_{PC} \big/ n} = \frac{PAR^i \times FPAR^i_{chl} \times \Phi^i_F}{\sum_{i=1}^{n} \left(PAR^i \times FPAR^i_{chl} \times \Phi^i_F \times f^i_{PC}\right) \big/ n} \tag{4}$$

Assuming PAR^i has negligible spatial variation at a single pixel (e.g., 5.6 × 3.5 km^2) or a small region (e.g., 0.2° × 0.2° grid) at the overpass time of the satellite on clear-sky days, PAR^i in the right term of Eq. (4) can cancel out. Therefore, $HSIF^i_{total}$ is obtained by combining Eqs. (1)–(4) as follows:

$$HSIF^i_{total} = LSIF_{obs} \times \frac{FPAR^i_{chl} \times \Phi^i_F}{\sum_{i=1}^{n} \left(FPAR^i_{chl} \times \Phi^i_F \times f^i_{PC}\right) \big/ n} \tag{5}$$

Note that individual SIF soundings are shown in Fig. 1B and thus the spatial pattern is noisy. To reduce the noise of a single $LSIF_{obs}$ retrieval, several $LSIF_{obs}$ should be averaged over space and/or time (Sun et al., 2018; Yu et al., 2019; Guanter et al., 2021; Doughty et al., 2022). We

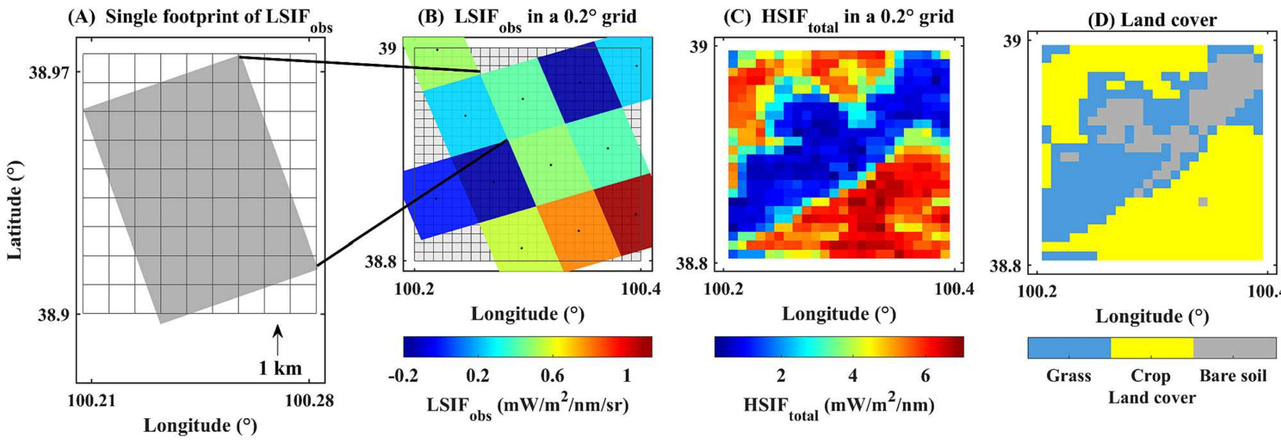

Fig. 1. A schematic of the downscaling framework: (A) a single TROPOMI $LSIF_{obs}$ footprint, (B) raw TROPOMI $LSIF_{obs}$ in a 0.2° grid, and (C) the spatially downscaled high resolution SIF_{total} ($HSIF_{total}$) in a 0.2° grid using Eq. (5). (D) Land cover from MCD12Q1. The smallest boxes represent the 1-km grid cells. The mismatch in magnitudes of SIF_{obs} and SIF_{total} was attributed to their different definitions.

aggregated at least six TROPOMI $LSIF_{obs}$ into a 0.2° grid for each day (e.g., 12 pixels in Fig. 1B), and then the averaged $LSIF_{obs}$ in each 0.2° grid was used in the right term of Eq. (5) to obtain the 1 km subpixel $HSIF_{total}$ (Fig. 1C). The spatial pattern of $HSIF_{total}$ was consistent with the land cover, with high values for crops (Fig. 1D). The value of six as the threshold was consistent with previous studies (Zhang et al., 2018a; Li and Xiao, 2019a). The calculations of $FPAR_{chl}$, f_{PC}, and Φ_F are presented in Section 2.3. Similarly, $HSIF_{obs}$ can be also estimated as the product of $HSIF_{total}$ and f_{PC}.

2.3. Calculations of $FPAR_{chl}$, f_{PC}, and Φ_F

Several satellite FPAR products are available (such as MODIS FPAR and MISR FPAR), but most of them represent the fraction of absorbed PAR by the whole canopy rather than chlorophyll alone. Following a recent study (Zhang et al., 2020d), we adopted Sentinel-3 OLCI FPAR data as $FPAR_{chl}$. More details about OLCI FPAR can refer to Gobron et al. (2022).

Many studies have established a link between reflectance and escape probability of fluorescence (Yang and van der Tol, 2018; Liu et al., 2019; Zeng et al., 2019; Liu et al., 2020; Zhang et al., 2020a; Zhang et al., 2020b). Here, the escape probability of fluorescence (f_{PC}) was calculated as follows:

$$f_{PC} = \frac{NIR_V}{\pi \times i_0 \times K_\lambda} \tag{6}$$

where NIR_V is the near infrared reflectance of vegetation (Badgley et al., 2017; Badgley et al., 2019), which is calculated with the reflectance at near-infrared (NIR) and red (R) bands:

$$NIR_V = \left(\frac{NIR - R}{NIR + R}\right) \times NIR \tag{7}$$

An identical sun-view geometry between SIF and reflectance is a mandatory condition for calculating f_{PC} (Yang and van der Tol, 2018). Therefore, NIR and R at a 1 km grid were simulated with the RossThick-LiSparseR (RTLSR) BRDF model (Lucht et al., 2000) at the same sun-target-viewing geometry as TROPOMI SIF. The parameters used to drive the RTLSR model are provided by the MCD19A3 BRDF/albedo product with a spatial resolution of 0.0083° × 0.0083° (close to 1 × 1 km^2) (Lyapustin et al., 2018). The canopy interception (i_0) was estimated with the G-function, leaf area index (LAI), clumping index (CI), and solar zenith angle (SZA) as below:

$$i_0 = 1 - exp(-G(SZA) \times LAI \times CI / cos(SZA)) \tag{8}$$

$$G(SZA) = \phi_1 + \phi_2 \times cos(SZA) \tag{9}$$

$$\phi_1 = 0.5 - 0.663\chi_L - 0.33{\chi_L}^2 \tag{10}$$

$$\phi_2 = 0.877(1 - 2\phi_1) \tag{11}$$

where the G-function is dependent on SZA and χ_L, which represents the departure of leaf angles from a random distribution. LAI data were obtained from MCD15A2H products (Myneni et al., 2015). CI data were obtained from (He et al., 2012). K_λ is the ratio of leaf albedo to the escape probability of fluorescence from the photosystem to the leaf surface. Following Zhang et al. (2021), χ_L is assigned biome-specific values (Table A1 in the appendix), and K_λ is set as 1.2 for far-red SIF. The uncertainty analysis on SIF_{total} can be found in a previous study (Zhang et al., 2021). Far-red SIF_{total} showed the improved relationship with GPP compared to SIF_{obs} when uncertainty levels for i_0 and NIR_V were <20% (Zhang et al., 2021). For example, the uncertainty level of i_0 derived from MODIS LAI was ~17% (Zhang et al., 2021).

The fluorescence correction vegetation index (FCVI) proposed by Yang et al. (2020) was used to calculate Φ_F as follows:

$$\Phi_F = \frac{\pi \times SIF_{obs}}{PAR \times FCVI} \tag{12}$$

$$FCVI = NIR - VIS \tag{13}$$

$$VIS = 0.331R + 0.424B + 0.246G \tag{14}$$

where *VIS* is the broadband visible reflectance over the 400–700 nm range, which was calculated as the weighted sum of reflectance at red (R), green (G), and blue (B) bands. The weights for these three bands were obtained from Liang (2001). Like NIR and R, the reflectance at the blue and green bands was also simulated with the RTLSR BRDF model to maintain identical sun-view geometry between SIF and FCVI. PAR was obtained from the solar shortwave radiation provided by ERA5 hourly data, using a conversion factor of 0.46 (Ryu et al., 2018). Following Yang et al. (2020), we did not consider grid cells with a FCVI <0.18. When estimating $HSIF_{total}$ using Eq. (5), high-resolution Φ_F was required. We first obtained the monthly-averaged Φ_F at the spatial resolution of 0.2° and then averaged all 0.2° Φ_F for each vegetation type in a 10° × 10° moving window. Finally, the vegetation-specific Φ_F was used to obtain Φ_F at 1 km spatial resolution within the 10° × 10° moving window. The vegetation type data were from MCD12Q1 vegetation type data under the International Geosphere-Biosphere Programme (IGBP) classification system. Following Frankenberg et al. (2011), some vegetation types were combined: evergreen needleleaf forest and deciduous needleleaf forest as needleleaf forest (NF); open and closed shrubland as shrubland (SHR), woody savannas and savannas (SAV) as SAV; croplands (CRO) and cropland/natural vegetation mosaics as CRO. The feasibility of the downscaling framework was first evaluated using a synthetic data based on the TROPOMI SIF (see Text A1 in the Appendix). The use of vegetation type-adjusted Φ_F had a small reduction in the accuracy of $HSIF_{total}$.

2.4. Evaluation of $HSIF_{total}$

Global $HSIF_{total}$ at 1 km was derived from TROPOMI SIF_{obs} and the estimate of the true $HSIF_{total}$ was evaluated using OCO-2 SIF due to the high spatial resolution of OCO-2. Although the footprint of OCO-2 SIF is ~1.25 km × 2.25 km, several adjacent retrievals should be averaged to reduce the retrieval uncertainty (Frankenberg et al., 2014; Sun et al., 2018; Doughty et al., 2022), thus reducing the spatial resolution. Therefore, both $HSIF_{total}$ and OCO-2 SIF_{total} were aggregated to 0.05° grid cells and then compared to each other. The 0.05° grid cells with at least six OCO-2 observations were used for comparison. OCO-2 SIF_{total} was calculated from OCO-2 SIF_{obs} as follows:

$$SIF_{total} = \frac{SIF_{obs}}{f_{PC}} \tag{15}$$

where f_{PC} was derived using Eq. (5), but the sun-view geometry information was from OCO-2 SIF itself. SIF_{obs} is sensitive to the sun-target-viewing geometry, so comparisons of SIF from OCO-2 and TROPOMI are most appropriate when the sun-sensor geometries are most similar (Köhler et al., 2018; Zhang et al., 2018b; Zhang and Zhang, 2023). Considering that both OCO-2 SIF_{total} and $HSIF_{total}$ were expected to be insensitive to the angular effects of SIF (Liu et al., 2020; Zhang et al., 2020b), they can be directly compared with each other by converting the instantaneous fluorescence to daily averages following the method of Frankenberg et al. (2011). Using this method can reduce the inconsistency of the local overpass time (or solar irradiance) between OCO-2 SIF and TROPOMI SIF. Following Zhang et al. (2018b), we compared the angular dependence of OCO-2 SIF_{obs} and SIF_{total} in the target mode around the FI-Hyy site. The angular dependence of SIF_{total} was clearly smaller than that of SIF_{obs} as indicated by the smaller coefficient of variation (CV = 0.08 vs 0.2, Fig. 2).

2.5. Flux tower GPP

Eddy covariance sites provide a direct measurement of the net ecosystem exchange of carbon dioxide (NEE) at half-hourly or hourly time steps, which is further partitioned into GPP and total ecosystem respiration based on the assumptions of the temperature dependence of respiration (Reichstein et al., 2005). The resulting half-hour GPP data were aggregated into 8-day GPP, which was compared to 8-day averaged $HSIF_{total}$. Half-hour GPP was not used because the instantaneous GPP was affected by measurement noise (Bodesheim et al., 2018). Since C_4 crops have higher light use efficiency than C_3 crops, the relationships between SIF and GPP were different from C_3 and C_4 crops. Therefore, we did not consider sites covered by C_4 crops.

In total, we used 135 sites from AmeriFlux, OzFlux, and European Flux after checking the data availability during 2018–2020. Site information is listed in Table A2 in the Appendix. We assessed the spatial mismatch effects on SIF-GPP relationships by comparing the relationships between tower GPP and $HSIF_{total}$ averaged over a different radius (from 1 km to 20 km with the interval of 1 km) around the tower. Linear models with or without an intercept have been used to link GPP and SIF (Sun et al., 2017; Zhang et al., 2020a). Therefore, these two types of linear models were used to link GPP and $HSIF_{total}$ in this study.

3. Results

In this section, we first showed the spatial and temporal patterns of Φ_F, which were related to the plant physiology. By considering the spatiotemporal variations in Φ_F, we generated the global $HSIF_{total}$ with a high resolution of 1 km and evaluated its accuracy using OCO-2 SIF. Next, we compared the relationships of tower GPP with $HSIF_{total}$ and $LSIF_{obs}$.

3.1. Spatial and temporal patterns of Φ_F

The spatial distribution of the Φ_F averaged over 2018 to 2020 and their seasonal variation (featured by the coefficient of variation, CV) is presented in Fig. 3. Clear spatial variations were shown across the globe, with high values being commonly observed for forest and crop and low values for shrub and grass. The white regions over land area indicated low vegetation cover in the arid and semiarid areas, where Φ_F cannot be well estimated with the FCVI-based approach (Yang et al., 2020). The seasonality of Φ_F also exhibited clear spatial variations. For example, the low-latitude tropical forest showed a weak seasonality, while northern Europe has a strong seasonality (Fig. 3B). Fig. 4 shows the seasonal variations of Φ_F for eight vegetation types in the Northern Hemisphere. SHR, SAV, GRA and CRO exhibited larger standard deviations of the Φ_F compared to forests (NF, EBF, DBF, and MF). These results indicated that there are stronger spatial heterogeneities in Φ_F for non-forests than forests. In addition, the seasonal variations of Φ_F were generally higher for DBF, MF, and GRA than for other vegetation types. The peak Φ_F commonly occurred during the peak growing season for DBF, MF and

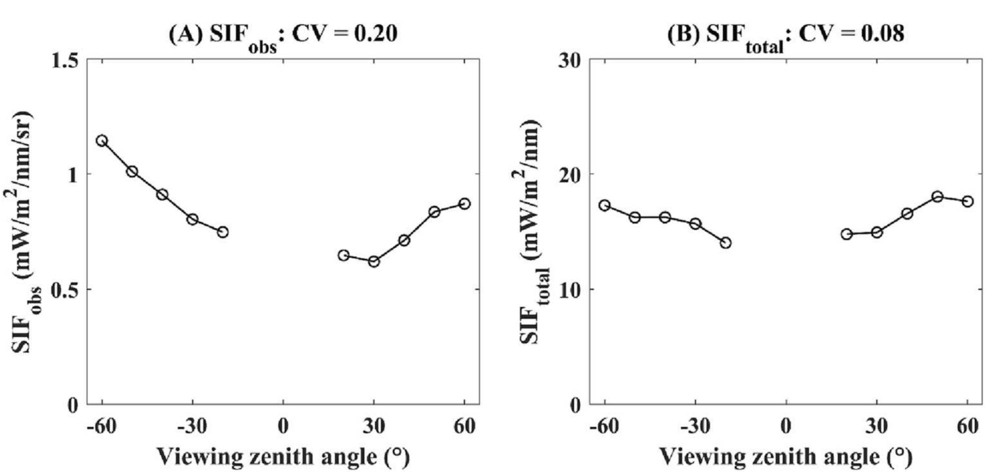

Fig. 2. The angular dependence of (A) SIF_{obs} and (B) SIF_{total} at the FI-Hyy site. Negative and positive viewing zenith angles respond to backward and forward directions, respectively. The data were obtained from OCO-2 SIF in the target mode on 1st July 2017. CV = coefficient of variation.

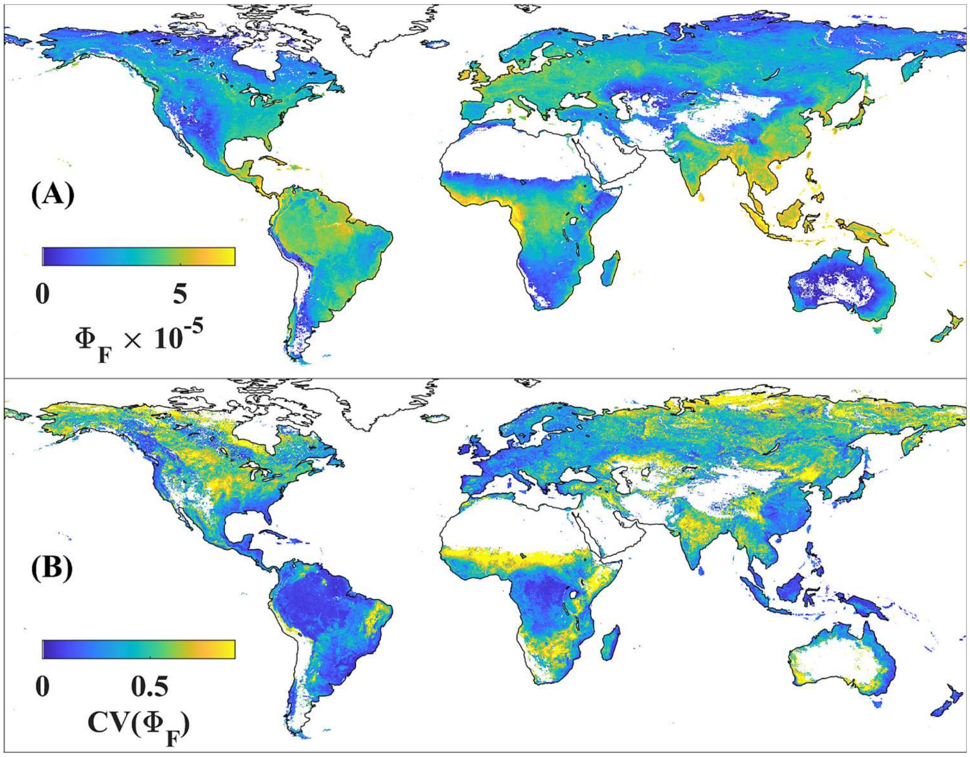

Fig. 3. The spatial distribution of fluorescence efficiency (Φ_F) at a spatial resolution of 0.2° averaged over 2018–2020 using Eq. (11) and their seasonal variations featured by the coefficient of variation (CV). The white region over land area indicated low vegetation cover in the arid and semiarid areas, where Φ_F cannot be well estimated with the FCVI-based approach.

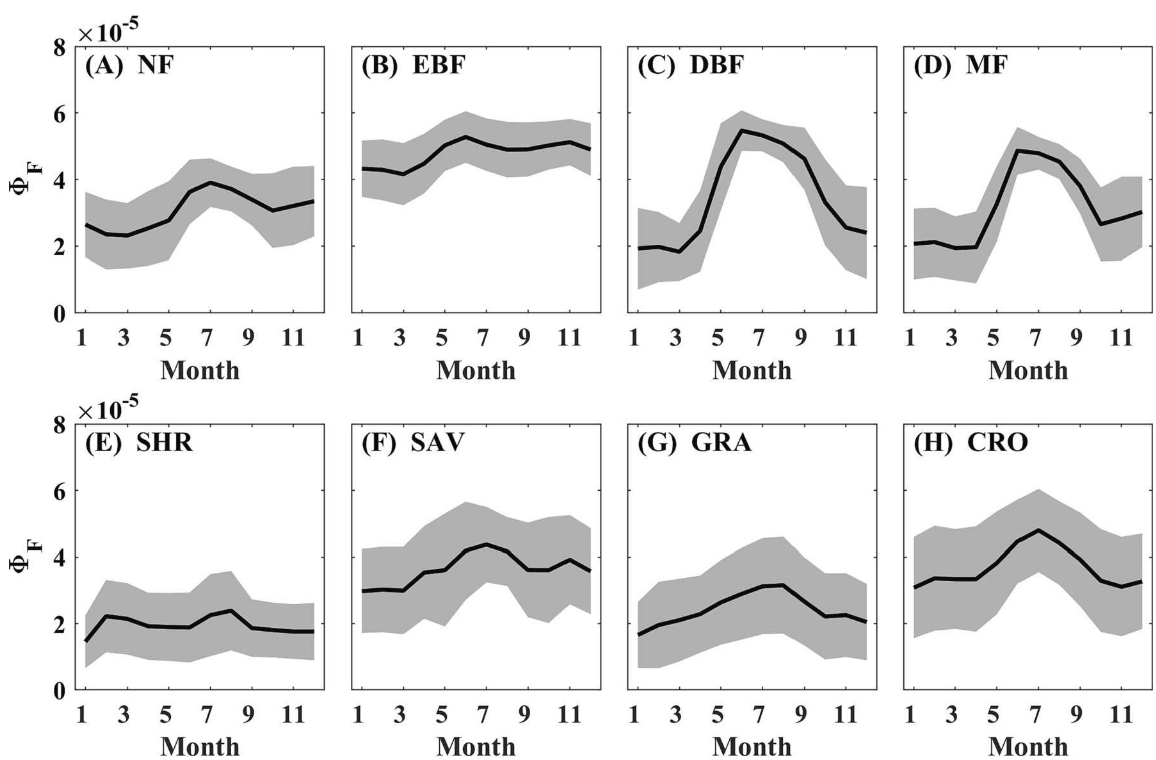

Fig. 4. Seasonal variations in fluorescence efficiency (Φ_F) for eight vegetation types in the Northern Hemisphere. The shaded region represents ± one standard deviation. CRO = cropland, SHR = shrubland, DBF = deciduous broadleaf forest, EBF = evergreen broadleaf forest, NF = needleleaf forest, GRA = grass, MF = mixed forest, OSH = open shrubland, and SAV = savanna.

GRA.

3.2. Evaluation of $HSIF_{total}$

The reliability of the global $HSIF_{total}$ was evaluated using OCO-2 SIF. The coefficient of determination (R^2) for OCO-2 SIF_{total} and $HSIF_{total}$ was 0.78, and the root mean squared error (RMSE) was 1.33 $mW/m^2/nm$ (Fig. 5A). We further compared R^2 and RMSE across different vegetation types and found that our $HSIF_{total}$ exhibited $R^2 > 0.6$ for most vegetation types (Fig. 5B). The R^2 between OCO-2 SIF_{total} and $HSIF_{total}$ was the highest for DBF ($R^2 > 0.8$), followed by MF and CRO. The lowest R^2 was observed for EBF, mainly arising from its low seasonality in photosynthesis and more clouds in tropics that reduced the SIF quality. The RMSE was <1.87 $mW/m^2/nm$ for all vegetation types (Fig. 5C). Although R^2 was clearly lower for EBF than for MF, EBF showed comparable RMSE with MF. Overall, these comparisons between $HSIF_{total}$ and OCO-2 SIF_{total} indicate that our $HSIF_{total}$ was accurate for EBF and other vegetation types.

3.3. The relationships between tower GPP and $HSIF_{total}$

We presented the global spatial patterns of f_{PC}, $LSIF_{obs}$ and $HSIF_{total}$ averaged over the days 200–230 of 2018 in Fig. 6. Clearly, the f_{PC} varied in space and higher values were observed in crops (such as the Corn Belt, a black box) and the southern boundary of Sahara Desert. In the Corn Belt, the f_{PC} was higher for crops than other surrounding vegetation types, such as DBF and SAV (Fig. A2). The high f_{PC} may partly determine the high SIF_{obs} for crops in the Corn Belt (Fig. 6B). Compared to the 0.2° $LSIF_{obs}$, the 1 km $HSIF_{total}$ showed more detailed spatial information. For example, river pixels with low SIF_{total} values were observed and can be well separated from surrounding vegetation pixels (Fig. 6C). In addition, crops showed comparable or even slightly lower SIF_{total} than DBF and SAV after correcting f_{PC} effects. When comparing the spatial distribution of $LSIF_{obs}$, lower values were observed in the European region (such as the red box) than in the Corn Belt (the black box) (Fig. 6B). This difference could be partly caused by the low f_{PC} for needleleaf forest (Fig. 6A). For $HSIF_{total}$ correcting the f_{PC} effect, comparable values were obtained between the European region and the Corn Belt (Fig. 6C).

We further compared the $HSIF_{total}$ with the tower GPP and evaluated the effect of spatial mismatch on their relationships. For comparison, both linear models with and without intercept were used. The slope and R^2 for the relationships between GPP and $HSIF_{total}$ extracted within a varying buffer (search radii from 1 km to 20 km surrounding individual towers) are shown in Fig. 7A-B. The slopes for GPP and $HSIF_{total}$ increased with the search radius regardless of the model with or without intercepts (Fig. 7A), which indicated that applying the slope at a 20 km search radius to upscale SIF to GPP could lead to higher GPP estimation than applying the slope at a 1 km search radius. Importantly, R^2 for GPP and $HSIF_{total}$ decreased with the search radius (Fig. 7B), which indicated that the larger mismatch in the footprint between GPP and SIF led to the weakened performance of the GPP ~ $HSIF_{total}$ model. In contrast, $HSIF_{obs}$ cannot reveal the spatial mismatch effects on GPP ~ SIF relationships (Fig. A3), which could be masked by the compound canopy structural and angular effects on SIF_{obs}. $HSIF_{total}$ at the smallest search radius (1 km) centered with EC towers had the most comparable footprint size with GPP. Thus, the R^2 (0.70) for GPP and $HSIF_{total}$ peaked at a 1 km searching radius (scattering density plot is shown in Fig. 7C). The R^2 was expected to rapidly increase as the radius decreased (Fig. 7B) because most non-forest sites have smaller flux footprints due to low tower heights <10 m (Table A2). In comparison, the relationship for GPP and $LSIF_{obs}$ averaged over a 10 km radius around the tower (R^2 = 0.64, Fig. 7D) was clearly poorer than that for GPP and $HSIF_{total}$ (Fig. 7C). These results indicated that a higher R^2 was promising under higher resolutions of SIF, such as FLEX SIF with a 300 m spatial resolution and after the correction for canopy structure effects.

We also explored the slope variations of regression models with and without intercepts among all individual sites. Regardless of whether the regression models had an intercept, the coefficient of variation (CV) was smaller for GPP ~ $HSIF_{total}$ (Fig. 8A&D) than for GPP ~ $LSIF_{obs}$ (Fig. 8B&E) and GPP ~ $HSIF_{obs}$ (Fig. 8C&F). In addition, the difference between the average R^2 for individual sites and the R^2 for lumped observations was rather small for GPP ~ $HSIF_{total}$ (Fig. A4), further supporting the consistent GPP-$HSIF_{total}$ relationship across sites.

We also evaluated the model performance of different SIF datasets in predicting GPP (R^2(GPP ~ $HSIF_{total}$), R^2(GPP ~ $LSIF_{obs}$) and R^2(GPP ~ $HSIF_{obs}$)) for individual sites. We found that more than half of sites had higher R^2 for GPP ~ $HSIF_{total}$ than for GPP ~ $LSIF_{obs}$ (Fig. 9A). R^2(GPP ~ $HSIF_{total}$) was also slightly higher than R^2(GPP ~ $HSIF_{obs}$), especially for these sites with low R^2(GPP ~ $HSIF_{obs}$) (Fig. 9B). These results indicated a more consistent GPP-$HSIF_{total}$ relationship across space, which was important for extrapolating site-level relationships to the global scale.

4. Discussion

4.1. Advantages and disadvantages of the $HSIF_{total}$ data

Many approaches have been proposed to downscale low-resolution SIF to high-resolution SIF, but most of these approaches are based on empirical models (Gentine and Alemohammad, 2018; Zhang et al., 2018a; Li and Xiao, 2019a; Yu et al., 2019; Wen et al., 2020; Hu et al., 2022; Ma et al., 2022). Downscaled SIF products have used MODIS surface reflectance, MODIS vegetation indices, and/or auxiliary data (such as PAR and air temperature), and the physiological information

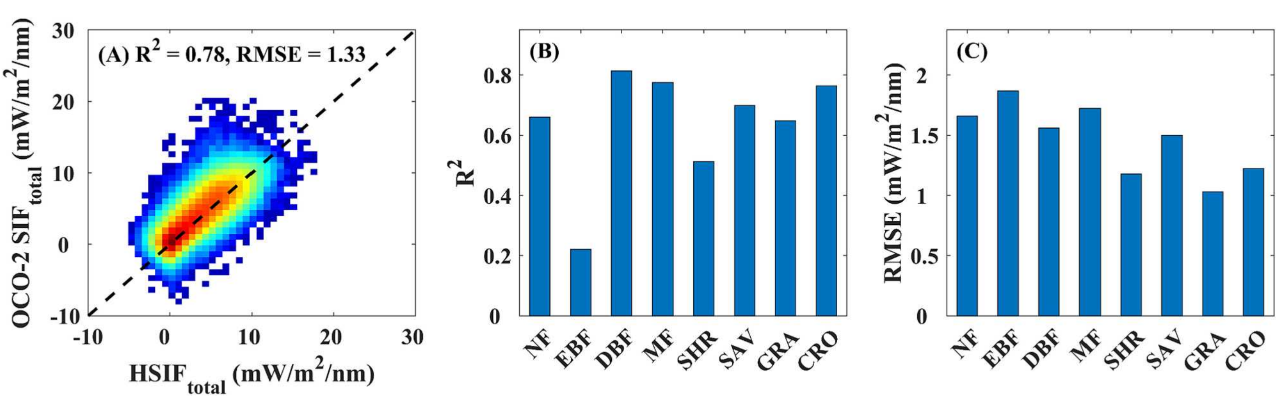

Fig. 5. (A) Density plots between OCO-2 SIF_{total} and $HSIF_{total}$. R^2 and RMSE represent the determination coefficient and root mean square error, respectively. (B) R^2 and (C) RMSE for OCO-2 SIF_{total} and $HSIF_{total}$ for each vegetation type. CRO = cropland, SHR = shrubland, DBF = deciduous broadleaf forest, EBF = evergreen broadleaf forest, NF = needleleaf forest, GRA = grass, MF = mixed forest, OSH = open shrubland, and SAV = savanna.

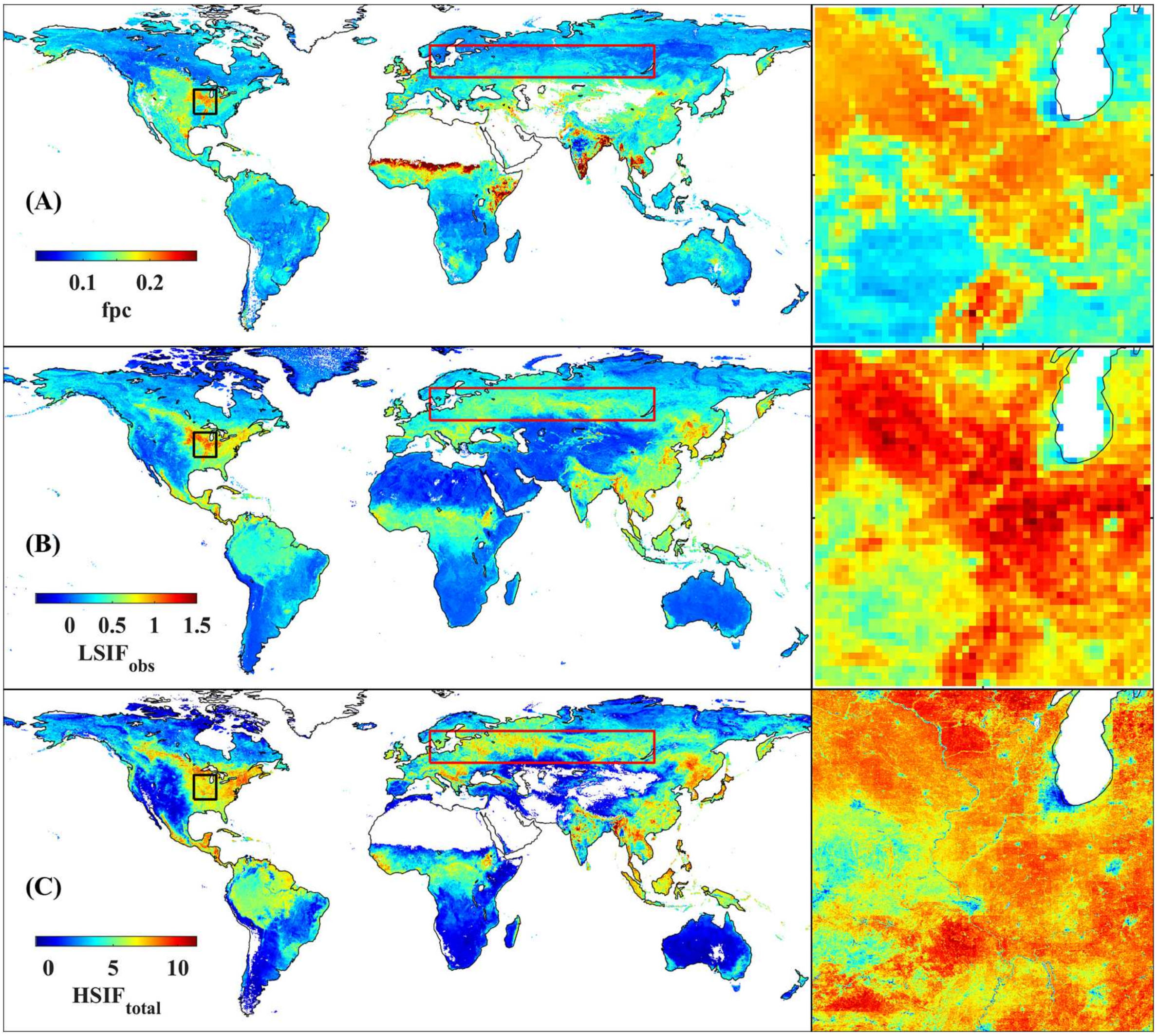

Fig. 6. The maps of averaged (A) escape probability of fluorescence (f_{PC}), (B) $LSIF_{obs}$ ($mW/m^2/nm/sr$) and (C) $HSIF_{total}$ ($mW/m^2/nm$) over the days 200–230 of 2018. A subregion (95°W-85°W, 35°N-45°N) is presented on the right for visualization. The magnitude mismatch between SIF_{obs} and SIF_{total} was attributed to their different definitions and the escape probability effect.

may not be well retained. Also, previous approaches still generate directional SIF_{obs}, which are thought to be affected by canopy structure (Guanter et al., 2012; Damm et al., 2015) and sun-target-viewing geometry (Zhang et al., 2018b).

Our straightforward physically based algorithm does not require any statistical assumptions and can avoid the fitting error of the empirical model. Based on spectral invariant theory (Knyazikhin et al., 2013; Yang and van der Tol, 2018), we can derive SIF_{total} by considering the escape probability of fluorescence into the downscale framework, as shown in Eq. (5). Meanwhile, the coarse-resolution physiological information from $LSIF_{obs}$ still exists in $HSIF_{total}$ due to the use of $LSIF_{obs}$ in this downscaling framework.

Due to this unique feature, our $HSIF_{total}$ can be generated only during the period when $LSIF_{obs}$ is available. In other words, our downscaled framework cannot reconstruct a long-term historic SIF. It should also be pointed out that the uncertainties in the input parameters for the calculation of the escape probability could affect the accuracy of $HSIF_{total}$. For example, the MODIS LAI product could suffer from saturation at dense canopies (Myneni et al., 2002), causing uncertainties in the calculation of i_0. The uncertainty in the MCD19A3 BRDF product could also cause uncertainty in the simulated NIR_V. All these aspects could affect the accuracy of the escape probability and hence $HSIF_{total}$. A SCOPE model-based study systematically evaluated the effects of uncertainties in NIR_V and i_0 on the GPP-SIF_{total} relationships and found that SIF_{total} improved the relationship with GPP than SIF_{obs} only when the uncertainties in NIR_V and i_0 were <20% (Zhang et al., 2021). Fortunately, current satellite LAI and BRDF products can improve the relationship between GPP and SIF_{obs}, supporting the reliability of our $HSIF_{total}$. In addition, the $HSIF_{total}$ evaluated with ground SIF measurements and OCO-2 SIF also confirmed its good accuracy (Figs. 4-5).

4.2. *Advantage of GPP estimation from $HSIF_{total}$*

The increasing number of eddy covariance towers over the past 30 years provides direct measurements as the *gold standard* of carbon fluxes and greatly improves the research of land–atmosphere interactions (Baldocchi, 2014). A large number of studies have established the relationships between ground GPP and satellite SIF, which are then used to scale SIF to GPP (Li and Xiao, 2019b; Zhang et al., 2020a; Zhang et al., 2020c). Limited by the coarse spatial resolution of satellite SIF products, satellite SIF is commonly averaged over a large radius around the tower, such as 25 km used in Verma et al. (2017), 2–25 km in Li et al. (2018), 10 km in Zhang et al. (2019), and 30 km in Zhang et al. (2020a). Recently, the footprint concept and the mismatch in footprints between in situ GPP and satellite observations have been recognized by several studies (Zhang et al., 2018a; Kong et al., 2022). For example, Zhang

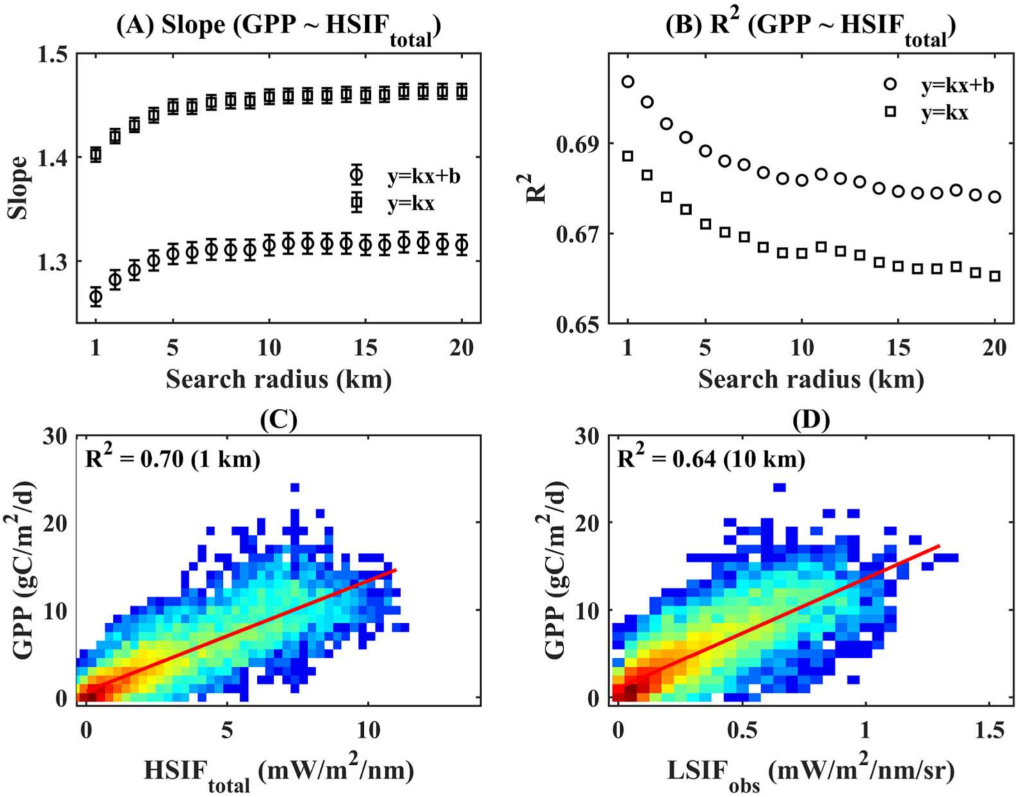

Fig. 7. (A) Slopes and (B) coefficient of determination (R^2) of relationships between 8-day GPP and $HSIF_{total}$ averaged from different search radii from all the sites. Both models with ($y = kx + b$) and without ($y = kx$) intercepts were used. (C) Scatter plot of GPP and $HSIF_{total}$ averaged from a 1 km search radius. (D) Scatter plot of GPP and TROPOMI $LSIF_{obs}$ averaged from a 10 km search radius. The error bar of slope represents the standard error, which was provided by the "fitlm" function in MATLAB. For each search radius, only one R^2 was reported, and the uncertainty of R^2 was not provided.

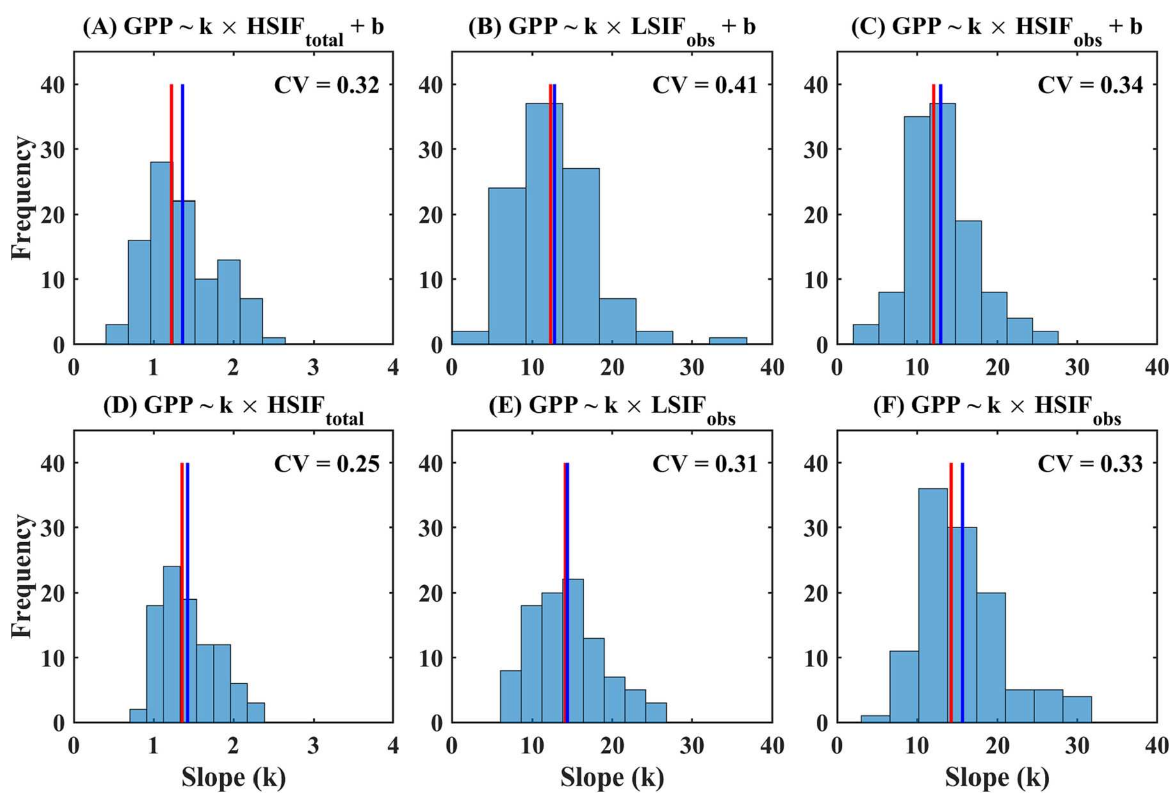

Fig. 8. Distributions of slopes of regression models with intercepts for GPP and (A) $HSIF_{total}$ at the 1 km search radius, (B) $LSIF_{obs}$ at the 10 km search radius, and (C) $HSIF_{obs}$ at the 1 km search radius. (D—F) is like (A-C) but for the regression model without intercepts. CV is the coefficient of variation. Red lines indicate the slope for lumped observations and blue lines indicate the average slope for all individual sites. (For interpretation of the references to colour in this figure legend, the reader is referred to the web version of this article.)

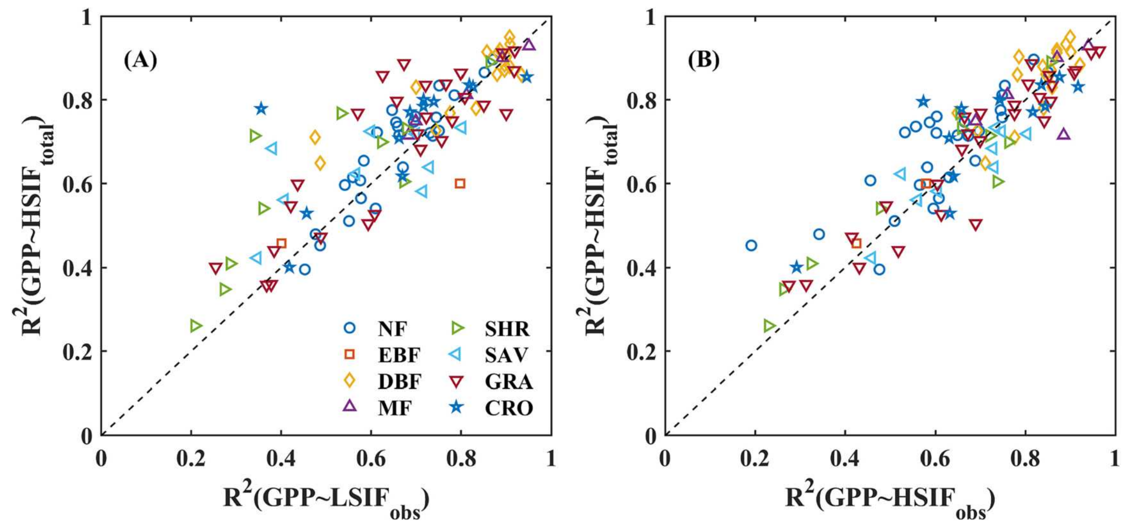

Fig. 9. Comparison of R^2(GPP ~ $HSIF_{total}$) at the 1 km search radius with (A) R^2(GPP ~ $LSIF_{obs}$) at the 10 km search radius and (B) R^2(GPP ~ HSIF) at the 1 km search radius for each site.

et al. (2018a) checked the homogeneity of NDVI as the growth condition around the flux sites and found that only 40 out of 166 sites were representative of a 5 km by 5 km area. To avoid the spatial mismatch or land heterogeneity effects on the SIF-GPP relationship, a previous screening of flux tower sites based on the homogeneity of MODIS land cover was also adopted by Zhang et al. (2020a).

If ignoring the spatial mismatch in the footprint between flux tower GPP and SIF, SIF-GPP relationships could be affected by the search radius or spatial mismatch between SIF and GPP due to land heterogeneity. Considering the potential of SIF for terrestrial GPP estimation and the global carbon cycle (Frankenberg et al., 2011; Sun et al., 2017), it is necessary to quantify the uncertainty in SIF-GPP models due to the spatial mismatch between tower GPP and satellite SIF. We demonstrate that the slope at the 1 km resolution is significantly ($p < 0.05$) different from that obtained at other search radii (Fig. 7A). The slope at the 1 km resolution could be closest to the "true slope" for the GPP and $HSIF_{total}$ models, which is also shown by the highest R^2 at the 1 km resolution (Fig. 7B). The increasing slope with the search radius is consistent with previous study (Fig. S4 in Li et al. (2018)), which indicated that GPP could be overestimated if using the slope established at a large search radius (> 1 km). We demonstrated the adverse effects of the spatial mismatch in the footprint between GPP and SIF on their relationships, which can be partially mitigated by our derived 1 km $HSIF_{total}$.

In addition to the high spatial resolution of $HSIF_{total}$, its insensitivity to canopy structure and sun-target-viewing geometry also contributed to its better relationship with GPP than $LSIF_{obs}$. For example, $HSIF_{total}$ still performed better than $HSIF_{obs}$ at the same search radius (Fig. 7B vs Fig. A3). Our results are supported by previous studies that reported that SIF_{total} performed better relationships with GPP than SIF_{obs} (Zhang et al., 2019; Lu et al., 2020; Liu et al., 2022). This is reasonable because the relationships between SIF_{obs} and GPP are affected by the varying escape probability of SIF across multiple biomes with distinct canopy structures (Zhang et al., 2018b; Liu et al., 2022). Using $HSIF_{total}$, it is possible to establish a nearly universal model for GPP estimation across biomes at least for C_3 plants, as suggested by Zhang et al. (2020a). This is further demonstrated by our results based on all individual sites (Fig. 8). However, the CV of slopes for GPP ~ $HSIF_{total}$ is higher across sites in this study than across biomes in Zhang et al. (2020a). This is consistent with the study by Zhang et al. (2018a) who also reported a larger cross-site variation of the GPP ~ SIF relationship than the cross-biome variation. These variations may lead to our moderate relationships between GPP ~ $HSIF_{total}$ for lumped observations (Fig. 7). More accurate estimation of SIF_{total} (Zhang et al., 2021) and the incorporations other physiological information (such as photochemical reflectance index) (Wang et al., 2020b) and environmental information (such as CO_2 concentration) (Qiu et al., 2020) could further improve the GPP estimation.

4.3. Potential applications of $HSIF_{total}$

The straightforward relationship between GPP and SIF has promoted the application of SIF in crop yield and productivity estimations (Guanter et al., 2014; Guan et al., 2016; Cai et al., 2019; Gao et al., 2020; Peng et al., 2020). However, a recent study pointed out that the coarse-resolution GOME-2 SIF does not perform significantly better than MODIS NDVI in predicting crop productivity (Sloat et al., 2021). This could be mainly caused by the contaminations from other mixed vegetation signals. Attributed to its higher resolution, $HSIF_{total}$ could outperform the original TROPOMI $LSIF_{obs}$ in estimating crop yield, which deserves further investigation. In addition, some researchers also assessed the European heatwave and drought on ecosystem productivity (Bastos et al., 2020; Wang et al., 2020a). The spatial resolution is not a limiting factor in these studies because climate anomalies commonly occur at large scales (>100 km). However, since $HSIF_{total}$ accounted for the canopy structural and angular effects in SIF_{obs}, it seems that "salt-and-pepper" noise would be less of a concern (Fig. A5). These results implied that $HSIF_{total}$ might outperform $LSIF_{obs}$ in monitoring heatwave and drought, which also deserves further investigation.

5. Conclusions

We proposed an approach to downscale low spatial resolution $LSIF_{obs}$ to high spatial resolution $HSIF_{total}$ and $HSIF_{obs}$ at 1 km spatial resolution using the law of energy conservation and spectral invariant theory. Compared to $LSIF_{obs}$, $HSIF_{total}$ not only captured more detailed spatial information but also mitigated the canopy structural and directional effects in SIF_{obs}. The reliability of our downscaled framework was well evaluated by independent OCO-2 SIF data. Using a comprehensive dataset from 135 flux towers, our results revealed that the spatial mismatch in the footprint between GPP and $HSIF_{total}$ affected their relationships. The slope for the $HSIF_{total}$ and GPP relationship decreased with the decreasing search radius (or conceptual footprint) of $HSIF_{total}$. The best $HSIF_{total}$-GPP model was obtained when $HSIF_{total}$ was averaged over a 1-km radius around the tower compared to other radii (>1 km). In addition, compared with $LSIF_{obs}$ and $HSIF_{obs}$, $HSIF_{total}$ showed a more consistent slope with GPP across all individual sites. $HSIF_{total}$ not only improved our understanding of spatial mismatch effects on the SIF-GPP relationships but also would advance SIF applications, such as crop yield estimation and stress monitoring.

Declaration of Competing Interest

The authors declare that they have no known competing financial interests or personal relationships that could have appeared to influence the work reported in this paper.

Data availability

AmeriFlux data was downloaded from http://ameriflux.ornl.gov/

European Flux was downloaded from http://www.europe-fluxdata.eu/

MODIS-related products were downloaded from https://search.earthdata.nasa.gov/search

OCO-2 SIF was downloaded from https://disc.gsfc.nasa.gov/

OzFlux was downloaded from http://www.ozflux.org.au/

Sentinel-3 OLCI FPAR was downloaded from TROPOMI SIF was downloaded from https://s5p-troposif.noveltis.fr/

Acknowledgments

This research was supported by the National Key Research and Development Program of China (2022YFF1301900), the National Natural Science Foundation of China (NSFC) (42125105, 42101320, 42071388), and the Fundamental Research Funds for the Central Universities (0209-14380115). The authors are thankful to the science team members who produced and managed the flux data (AmeriFlux, OzFlux, and European Flux) and remote sensing products used in this study. Funding for AmeriFlux data resources was provided by the U.S. Department of Energy's Office of Science. The tower height was provided by the principal investment of each flux tower site. We greatly appreciate the anonymous reviewers for their insightful and constructive comments that helped us to improve our manuscript.

Appendix A. Appendix

Table A1
Values of biome-specific χ_L.

Vegetation ID	Description	χ_L
NF	Needleleaf forest	0.01
EBF	Evergreen broadleaf forest	0.1
DBF	Deciduous broadleaf forest	0.25
MF	Mixed forest	0.25
SHR	Shrub	0.25
SAV	Savanna	0.25
GRA	Grass	−0.3
CRO	Crop	−0.3

A.1. Text A1. Evaluation of the downscaling approach using a synthetic data

We used TROPOMI SIF_{obs} at 0.2° as the high-resolution data and aggregated this TROPOMI SIF_{obs} to 1°. Then, we applied the downscaling process to the 1° TROPOMI SIF_{obs} and obtained the 0.2° SIF_{total}. First, the true Φ_F at 0.2° was used in the downscaling process for comparison. The downscaled SIF_{total} and true SIF_{total} at 0.2° showed high consistency with the R^2 of 0.98 (Fig. A1). Next, we also used the Φ_F adjusted using vegetation types in the downscaling process and obtained the downscaled SIF, which still had a high consistency with the true SIF ($R^2 = 0.93$, Fig. A1B). We agree that the use of vegetation type-adjusted Φ_F slightly decreased the performance of this downscaling method (R^2 from 0.98 to 0.93). However, the R^2 was still high using the vegetation type-adjusted Φ_F, indicating that the downscaling framework using Eq. (5) is feasible.

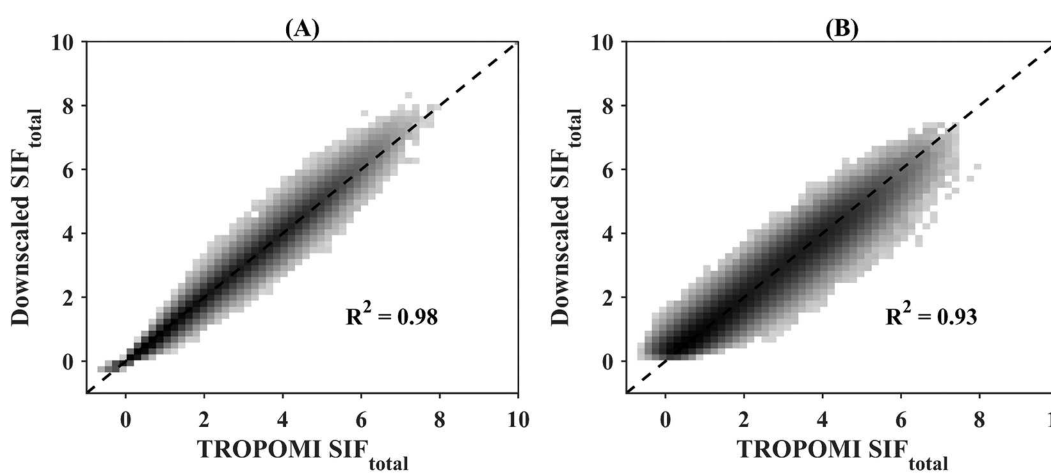

Fig. A1. (A) Density plots between TROPOMI SIF_{total} and downscaled SIF_{total} using the true Φ_F based on a synthetic data. (B) Similar to (A) but using the Φ_F adjusted using vegetation types.

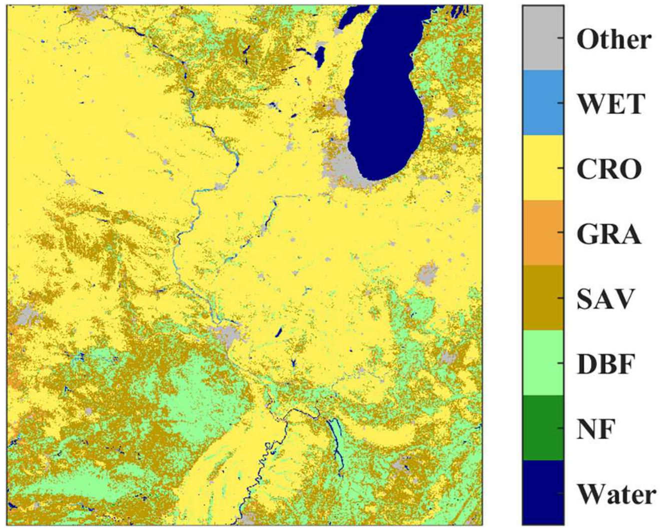

Fig. A2. MODIS land cover in the Corn belt (95°W-85°W, 35°N-45°N).

Table A2
Flux sites used in this study during 2018–2020. CRO = cropland, CSH = close shrubland, DBF = deciduous broadleaf forest, EBF = evergreen broadleaf forest, ENF = evergreen needleleaf forest, GRA = grass, MF = mixed forest, OSH = open shrubland, SAV = savanna, WET = wetland, and WSA = wood savanna.

Site ID	Latitude (°)	Longitude (°)	IGBP	Tower height (m)	References
AU-ASM	−22.2828	133.2493	ENF	13.7	(Cleverly et al., 2013)
AU-Cpr	−34.0027	140.5877	SAV	20.0	(Meyer et al., 2015)
AU-Cum	−33.6152	150.7236	EBF	30.0	(Beringer et al., 2016)
AU-Das	−14.1592	131.3881	SAV	23.0	(Hutley et al., 2011)
AU-Dry	−15.2588	132.3706	SAV	15.0	(Cernusak et al., 2011)
AU-Gin	−31.3764	115.7139	WSA	15.0	–
AU-GWW	−30.1913	120.6541	SAV	36.0	(Prober et al., 2012)
AU-How	−12.4952	131.1501	WSA	23.0	(Beringer et al., 2007)
AU-Lit	−13.1790	130.7945	SAV	30.0	(Beringer et al., 2016)
AU-Lon	−23.5233	144.3104	GRA	2.5	–
AU-Rgf	−32.5061	116.9668	CRO	10.0	–
AU-Stp	−17.1507	133.3502	GRA	5.0	–
AU-TUM	−35.6566	148.1517	EBF	70.0	(Leuning et al., 2005)
AU-Ync	−34.9893	146.2907	GRA	20.0	(Yee et al., 2015)
BE-Bra	51.3076	4.5198	MF	33.0	(Janssens et al., 2001)
BE-Lon	50.5516	4.7461	CRO	2.1	(Moureaux et al., 2006)
BE-Vie	50.3050	5.9981	MF	51.0	(Aubinet et al., 2001)
CA-ER1	43.6405	−80.4123	CRO	2.3	–
CH-Cha	47.2102	8.4104	GRA	2.4	–
CH-Dav	46.8153	9.8559	ENF	35.0	(Zielis et al., 2014)
CH-Fru	47.1158	8.5378	GRA	2.5	(Imer et al., 2013)
CH-Lae	47.4781	8.3650	MF	47.0	(Etzold et al., 2011)
CZ-BK1	49.5021	18.5369	ENF	25.0	(Acosta et al., 2013)
DE-Geb	51.1001	10.9143	CRO	3.0	(Anthoni et al., 2004)
DE-Gri	50.9500	13.5126	GRA	3.0	(Hussain et al., 2011)
DE-Hai	51.0792	10.4530	DBF	45.0	(Knohl et al., 2003)
DE-Kli	50.8931	13.5224	CRO	3.5	–
DE-Obe	50.7867	13.7213	ENF	30.0	–
DE-RuR	50.6219	6.3041	GRA	–	(Post et al., 2015)
DE-Tha	50.9626	13.5652	ENF	42.0	(Gruenwald and Bernhofer, 2007)
DK-Sor	55.4859	11.6446	DBF	43.0	(Pilegaard and Ibrom, 2020)
ES-Abr	38.7018	−6.7859	SAV	15.0	(Luo et al., 2018)
ES-LM1	39.9427	−5.7787	SAV	15.0	(El-Madany et al., 2018)
ES-LM2	39.9346	−5.7759	SAV	15.0	(El-Madany et al., 2018)
FI-Hyy	61.8474	24.2948	ENF	27.0	(Ilvesniemi et al., 2009)
FI-Var	67.7549	29.6100	ENF	16.6	–
FR-Fon	48.4764	2.7801	DBF	37.0	(Delpierre et al., 2016)
FR-Hes	48.6741	7.0647	DBF	27.0	–
FR-LGt	47.3229	2.2838	WET	2.4	–
FR-Pue	43.7413	3.5957	EBF	12.0	(Rambal et al., 2004)
IL-Yat	31.3450	35.0520	ENF	19.0	–
IT-SR2	43.7320	10.2910	ENF	24.3	(Hoshika et al., 2017)
IT-Tor	45.8444	7.5781	GRA	2.5	(Galvagno et al., 2013)

(continued on next page)

Table A2 (*continued*)

Site ID	Latitude (°)	Longitude (°)	IGBP	Tower height (m)	References
RU-Fy2	56.4476	32.9019	ENF	44.0	(Kurbatova et al., 2008)
RU-Fyo	56.4615	32.9221	ENF	31.0	(Milyukova et al., 2002)
SE-Nor	60.0865	17.4795	ENF	33.0	–
US-ALQ	46.0308	−89.6067	WET	2.4	–
US-ARM	36.6058	−97.4888	CRO	4.6	(Fischer et al., 2007)
US-BRG	39.2167	−86.5406	GRA	3.0	–
US-CS1	44.1031	−89.5379	CRO	2.5	–
US-CS2	44.1467	−89.5002	ENF	32.0	–
US-CS3	44.1394	−89.5727	CRO	2.5	–
US-CS4	44.1597	−89.5475	CRO	2.5	–
US-DFC	43.3448	−89.7117	CRO	30.0	–
US-GLE	41.3665	−106.2399	ENF	22.7	(Frank et al., 2014)
US-Ha1	42.5378	−72.1715	DBF	29.0	(Urbanski et al., 2007)
US-Ha2	42.5393	−72.1779	ENF	29.0	–
US-HB1	33.3455	−79.1957	WET	3.9	–
US-HB2	33.3242	−79.2440	ENF	29.9	–
US-HB3	33.3482	−79.2322	ENF	4.1	–
US-HBK	43.9397	−71.7181	DBF	32.0	–
US-Hn2	46.6889	−119.4641	GRA	2.5	(Missik et al., 2019)
US-Hn3	46.6878	−119.4614	OSH	2.5	(Missik et al., 2019)
US-Ho1	45.2041	−68.7402	ENF	31.0	–
US-ICs	68.6058	−149.3110	WET	2.2	–
US-KFS	39.0561	−95.1907	GRA	3.0	–
US-Kon	39.0824	−96.5603	GRA	3.0	–
US-KS3	28.7084	−80.7427	WET	2.9	–
US-Los	46.0827	−89.9792	WET	10.2	(Sulman et al., 2009)
US-Me2	44.4523	−121.5574	ENF	33.0	(Irvine et al., 2008)
US-Me6	44.3233	−121.6078	ENF	12.0	(Ruehr et al., 2012)
US-MMS	39.3232	−86.4131	DBF	46.0	(Dragoni et al., 2011)
US-Mpj	34.4384	−106.2377	OSH	9.3	–
US-MtB	32.4167	−110.7255	ENF	30.0	–
US-NC2	35.8030	−76.6685	ENF	23.0	–
US-NC3	35.7990	−76.6560	ENF	10.0	–
US-NGC	64.8614	−163.7008	GRA	–	–
US-NR1	40.0329	−105.5464	ENF	21.5	(Monson et al., 2002)
US-ONA	27.3836	−81.9509	GRA	2.7	–
US-Rls	43.1439	−116.7356	CSH	2.1	(Flerchinger et al., 2019)
US-Rms	43.0645	−116.7486	CSH	2.1	(Flerchinger et al., 2019)
US-Ro4	44.6781	−93.0723	GRA	2.6	–
US-Ro5	44.6910	−93.0576	CRO	2.5	–
US-Ro6	44.6946	−93.0578	CRO	2.3	–
US-Rwf	43.1207	−116.7231	CSH	3.5	(Flerchinger et al., 2019)
US-Rws	43.1675	−116.7132	OSH	2.1	(Flerchinger et al., 2019)
US-Seg	34.3623	−106.7019	GRA	3.1	–
US-Ses	34.3349	−106.7442	OSH	3.1	–
US-Sne	38.0369	−121.7547	GRA	5.4	–
US-Snf	38.0402	−121.7272	GRA	3.5	–
US-SRG	31.7894	−110.8277	GRA	3.3	(Scott et al., 2015)
US-SRM	31.8214	−110.8661	WSA	7.8	(Scott et al., 2009)
US-SRS	31.8173	−110.8508	WSA	7.0	(Pierini et al., 2014)
US-Syv	46.2420	−89.3477	MF	36.0	(Sulman et al., 2009)
US-Ton	38.4309	−120.9660	WSA	23.5	(Ma et al., 2007)
US-Uaf	64.8663	−147.8555	ENF	6.0	(Ueyama et al., 2014)
US-UMd	45.5625	−84.6975	DBF	32.0	–
US-Var	38.4133	−120.9508	GRA	2.0	(Ma et al., 2007)
US-Vcm	35.8884	−106.5321	ENF	23.6	–
US-Vcp	35.8624	−106.5974	ENF	23.8	–
US-WCr	45.8059	−90.0799	DBF	29.6	(Sulman et al., 2009)
US-Whs	31.7438	−110.0522	OSH	6.5	(Scott et al., 2015)
US-Wjs	34.4255	−105.8615	SAV	8.0	–
US-Wkg	31.7365	−109.9419	GRA	6.4	(Scott et al., 2010)
US-xAB	45.7624	−122.3303	ENF	19.0	–
US-xAE	35.4106	−99.0588	GRA	8.0	–
US-xBL	39.0603	−78.0716	DBF	8.0	–
US-xBN	65.1540	−147.5026	ENF	19.0	–
US-xBR	44.0639	−71.2873	DBF	35.0	–
US-xCL	33.4012	−97.5700	GRA	22.0	–
US-xDC	47.1617	−99.1066	GRA	8.0	–
US-xDL	32.5417	−87.8039	MF	42.0	–
US-xDS	28.1250	−81.4362	CVM	8.0	–
US-xGR	35.6890	−83.5019	DBF	45.0	–
US-xHA	42.5369	−72.1727	DBF	39.0	–
US-xHE	63.8757	−149.2133	OSH	9.0	–
US-xJE	31.1948	−84.4686	ENF	42.0	–

(continued on next page)

Table A2 (*continued*)

Site ID	Latitude (°)	Longitude (°)	IGBP	Tower height (m)	References
US-xJR	32.5907	−106.8425	OSH	8.0	–
US-xKA	39.1104	−96.6129	GRA	8.0	–
US-xKZ	39.1008	−96.5631	GRA	8.0	–
US-xML	37.3783	−80.5248	DBF	29.0	–
US-xNG	46.7697	−100.9154	GRA	8.0	–
US-xNQ	40.1776	−112.4524	OSH	8.0	–
US-xRM	40.2759	−105.5459	ENF	25.0	–
US-xRN	35.9641	−84.2826	DBF	39.0	–
US-xSE	38.8901	−76.5600	DBF	62.0	–
US-xSL	40.4619	−103.0293	CRO	8.0	–
US-xST	45.5089	−89.5864	DBF	22.0	–
US-xTA	32.9505	−87.3933	ENF	35.0	–
US-xTL	68.6611	−149.3705	WET	9.0	–
US-xTR	45.4937	−89.5857	DBF	36.0	–
US-xUK	39.0404	−95.1921	DBF	35.0	–
US-xUN	46.2339	−89.5373	MF	39.0	–
US-xWD	47.1282	−99.2414	GRA	8.0	–
US-xWR	45.8205	−121.9519	ENF	74.0	–
US-xYE	44.9535	−110.5391	ENF	18.0	–

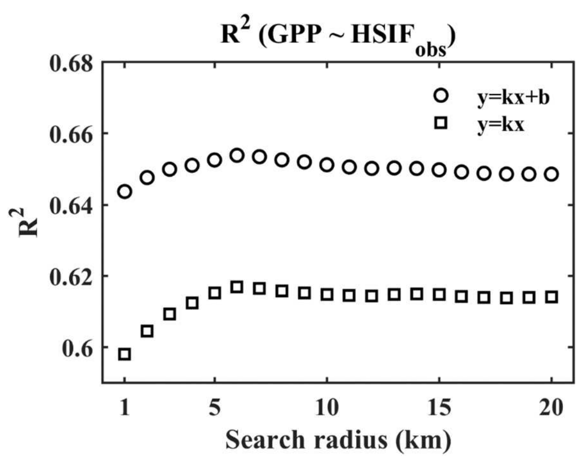

Fig. A3. Coefficient of determination (R^2) of relationships between daily 8-day GPP and $HSIF_{obs}$ averaged from different search radii. Both models with (y = kx + b) and without (y = kx) intercepts were used.

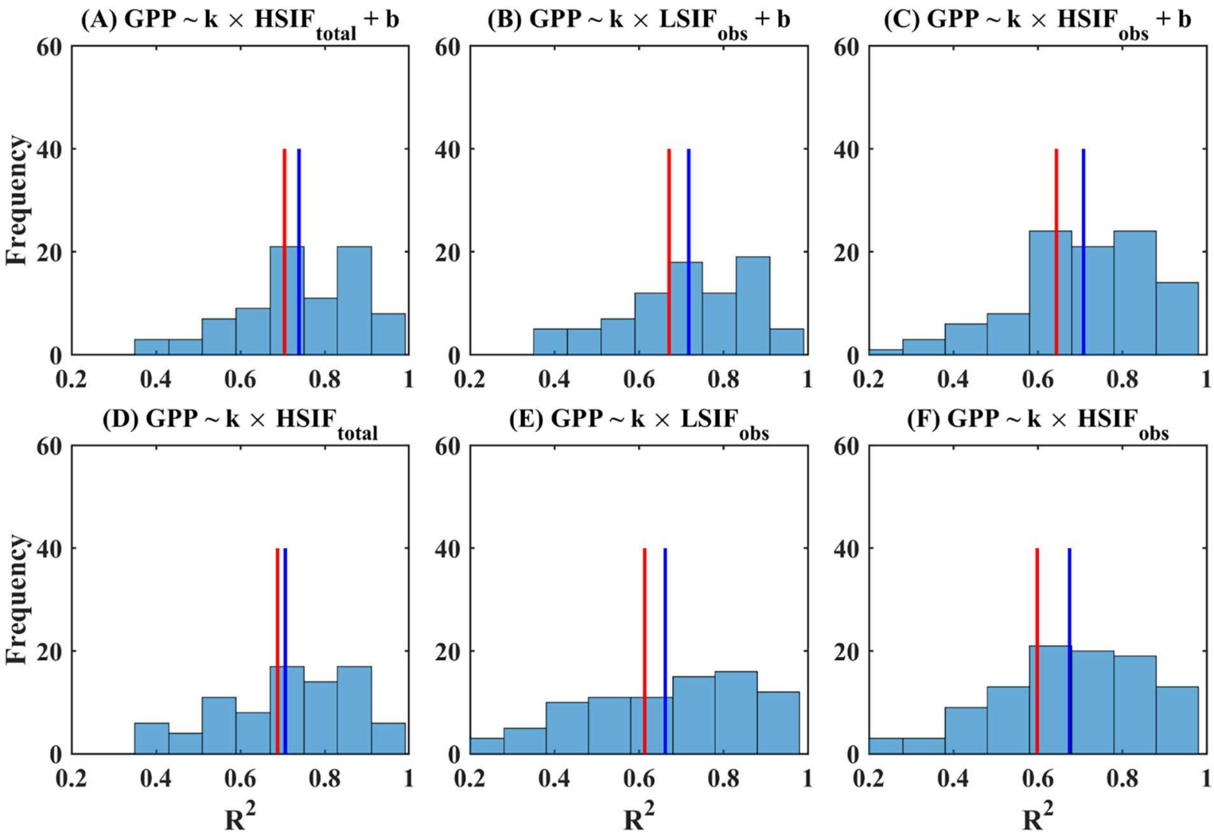

Fig. A4. Similar to Fig. 8 but for R^2.

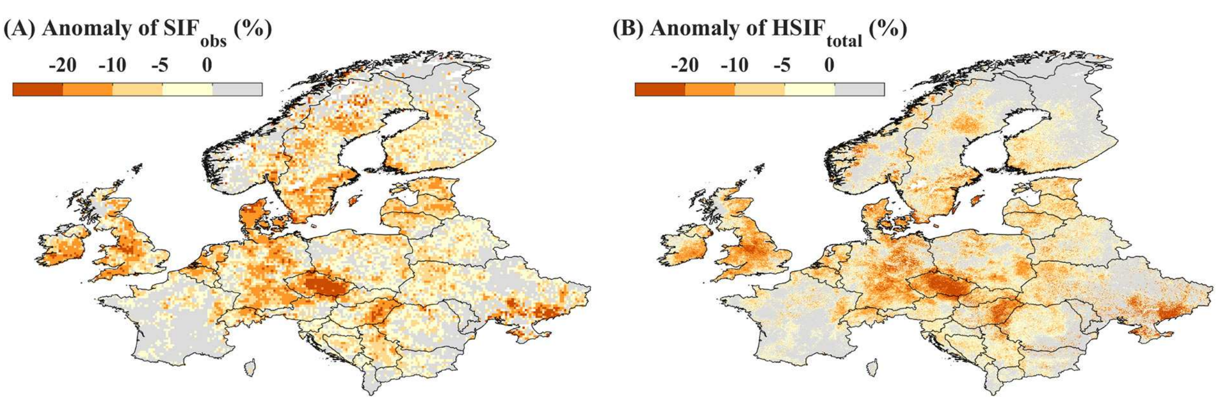

Fig. A5. Anomaly of (A) $LSIF_{obs}$ and (B) $HSIF_{total}$ over parts of Europe during the 2018 summer heatwave (June, July, August). The anomaly was calculated as the relative difference (%) between the values in 2018 and the averaged values from 2019 to 2021.

References

Acosta, M., Pavelka, M., Montagnani, L., Kutsch, W., Lindroth, A., Juszczak, R., Janou, D., 2013. Soil surface CO2 efflux measurements in Norway spruce forests: comparison between four different sites across Europe - from boreal to alpine forest. Geoderma 192, 295–303. https://doi.org/10.1016/j.geoderma.2012.08.027.

Anthoni, P., Knohl, A., Rebmann, C., Freibauer, A., Mund, M., Ziegler, W., et al., 2004. Forest and agricultural land-use-dependent CO2 exchange in Thuringia, Germany. Glob. Chang. Biol. 10, 2005–2019. https://doi.org/10.1111/j.1365-2486.2004.00863.x.

Aubinet, M., Chermanne, B., Vandenhaute, M., Longdoz, B., Yernaux, M., Laitat, E., 2001. Long term carbon dioxide exchange above a mixed forest in the belgian Ardennes. Agric. For. Meteorol. 108, 293–315. https://doi.org/10.1016/S0168-1923(01)00244-1.

Badgley, G., Anderegg, L.D.L., Berry, J.A., Field, C.B., 2019. Terrestrial gross primary production: using NIRV to scale from site to globe. Glob. Chang. Biol. 25, 3731–3740. https://doi.org/10.1111/gcb.14729.

Badgley, G., Field, C.B., Berry, J.A., 2017. Canopy near-infrared reflectance and terrestrial photosynthesis. Sci. Adv. 3, e1602244 https://doi.org/10.1126/sciadv.1602244.

Baldocchi, D.D., 2014. Measuring fluxes of trace gases and energy between ecosystems and the atmosphere – the state and future of the eddy covariance method. Glob. Chang. Biol. 20, 3600–3609. https://doi.org/10.1111/gcb.12649.

Bastos, A., Ciais, P., Friedlingstein, P., Sitch, S., Pongratz, J., Fan, L., 2020. Direct and seasonal legacy effects of the 2018 heat wave and drought on European ecosystem productivity. Sci. Adv. 6, eaba2724 https://doi.org/10.1126/sciadv.aba2724.

Beringer, J., Hutley, L.B., McHugh, I., Arndt, S.K., Campbell, D., Cleugh, H.A., et al., 2016. An introduction to the australian and New Zealand flux tower network – OzFlux. Biogeosciences 13, 5895–5916. https://doi.org/10.5194/bg-13-5895-2016.

Beringer, J., Hutley, L.B., Tapper, N.J., Cernusak, L.A., 2007. Savanna fires and their impact on net ecosystem productivity in North Australia. Glob. Chang. Biol. 13, 990–1004. https://doi.org/10.1111/j.1365-2486.2007.01334.x.

Bodesheim, P., Jung, M., Gans, F., Mahecha, M.D., Reichstein, M., 2018. Upscaled diurnal cycles of land–atmosphere fluxes: a new global half-hourly data product. Earth Syst. Sci. Data 10, 1327–1365. https://doi.org/10.5194/essd-10-1327-2018.

Cai, Y., Guan, K., Lobell, D., Potgieter, A.B., Wang, S., Peng, J., et al., 2019. Integrating satellite and climate data to predict wheat yield in Australia using machine learning approaches. Agric. For. Meteorol. 274, 144–159. https://doi.org/10.1016/j.agrformet.2019.03.010.

Cernusak, L.A., Hutley, L.B., Beringer, J., Holtum, J.A., Turner, B.L., 2011. Photosynthetic physiology of eucalypts along a sub-continental rainfall gradient in northern Australia. Agric. For. Meteorol. 151, 1462–1470. https://doi.org/10.1016/j.agrformet.2011.01.006.

Chu, H., Luo, X., Ouyang, Z., Chan, W.S., Dengel, S., Biraud, S.C., et al., 2021. Representativeness of Eddy-covariance flux footprints for areas surrounding AmeriFlux sites. Agric. For. Meteorol. 301–302, 108350 https://doi.org/10.1016/j.agrformet.2021.108350.

Cleverly, J., Boulain, N., Villalobos-Vega, R., Grant, N., Faux, R., Wood, C., et al., 2013. Dynamics of component carbon fluxes in a semi-arid acacia woodland, Central Australia. J. Geophys. Res. Biogeosci. 118, 1168–1185. https://doi.org/10.1002/jgrg.20101.

Damm, A., Guanter, L., Paul-Limoges, E., van der Tol, C., Hueni, A., Buchmann, N., et al., 2015. Far-red sun-induced chlorophyll fluorescence shows ecosystem-specific relationships to gross primary production: an assessment based on observational and modeling approaches. Remote Sens. Environ. 166, 91–105. https://doi.org/10.1016/j.rse.2015.06.004.

Delpierre, N., Berveiller, D., Granda, E., Dufrêne, E., 2016. Wood phenology, not carbon input, controls the interannual variability of wood growth in a temperate oak forest. New Phytol. 210, 459–470. https://doi.org/10.1111/nph.13771.

Doughty, R., Köhler, P., Frankenberg, C., Magney, T.S., Xiao, X., Qin, Y., 2019. TROPOMI reveals dry-season increase of solar-induced chlorophyll fluorescence in the Amazon forest. Proc. Natl. Acad. Sci. USA, 201908157. https://doi.org/10.1073/pnas.1908157116.

Doughty, R., Kurosu, T.P., Parazoo, N., Köhler, P., Wang, Y., Sun, Y., Frankenberg, C., 2022. Global GOSAT, OCO-2, and OCO-3 solar-induced chlorophyll fluorescence datasets. Earth Syst. Sci. Data 14, 1513–1529. https://doi.org/10.5194/essd-14-1513-2022.

Dragoni, D., Schmid, H.P., Wayson, C.A., Potter, H., Grimmond, C.S.B., Randolph, J.C., 2011. Evidence of increased net ecosystem productivity associated with a longer vegetated season in a deciduous forest in south-Central Indiana, USA. Glob. Chang. Biol. 17, 886–897. https://doi.org/10.1111/j.1365-2486.2010.02281.x.

Drusch, M., Moreno, J., Del Bello, U., Franco, R., Goulas, Y., Huth, A., et al., 2016. The fluorescence explorer mission concept—ESA's earth explorer 8. IEEE Trans. Geosci. Remote Sens. 55, 1273–1284. https://doi.org/10.1109/TGRS.2016.2621820.

Du, S., Liu, L., Liu, X., Zhang, X., Zhang, X., Bi, Y., Zhang, L., 2018. Retrieval of global terrestrial solar-induced chlorophyll fluorescence from TanSat satellite. Sci. Bull. 63, 1502–1512. https://doi.org/10.1016/j.scib.2018.10.003.

Duveiller, G., Cescatti, A., 2016. Spatially downscaling sun-induced chlorophyll fluorescence leads to an improved temporal correlation with gross primary productivity. Remote Sens. Environ. 182, 72–89. https://doi.org/10.1016/j.rse.2016.04.027.

Duveiller, G., Filipponi, F., Walther, S., Köhler, P., Frankenberg, C., Guanter, L., Cescatti, A., 2020. A spatially downscaled sun-induced fluorescence global product for enhanced monitoring of vegetation productivity. Earth Syst. Sci. Data 12, 1101–1116. https://doi.org/10.5194/essd-12-1101-2020.

El-Madany, T.S., Reichstein, M., Perez-Priego, O., Carrara, A., Moreno, G., Pilar Martín, M., et al., 2018. Drivers of spatio-temporal variability of carbon dioxide and energy fluxes in a Mediterranean savanna ecosystem. Agric. For. Meteorol. 262, 258–278. https://doi.org/10.1016/j.agrformet.2018.07.010.

Etzold, S., Ruehr, N.K., Zweifel, R., Dobbertin, M., Zingg, A., Pluess, P., et al., 2011. The carbon balance of two contrasting mountain forest ecosystems in Switzerland: similar annual trends, but seasonal differences. Ecosystems 14, 1289–1309. https://doi.org/10.1007/s10021-011-9481-3.

Fischer, M.L., Billesbach, D.P., Berry, J.A., Riley, W.J., Torn, M.S., 2007. Spatiotemporal variations in growing season exchanges of CO2, H2O, and sensible heat in agricultural fields of the southern great plains. Earth Interact. 11, 1–21. https://doi.org/10.1175/ei231.1.

Flerchinger, G.N., Fellows, A.W., Seyfried, M.S., Clark, P.E., Lohse, K.A., 2019. Water and carbon fluxes along an elevational gradient in a sagebrush ecosystem. Ecosystems 23, 246–263. https://doi.org/10.1007/s10021-019-00400-x.

Frank, J.M., Massman, W.J., Ewers, B.E., Huckaby, L.S., Negrón, J.F., 2014. Ecosystem CO2/H2O fluxes are explained by hydraulically limited gas exchange during tree mortality from spruce bark beetles. J.Geophys. Res. Biogeosci. 119, 1195–1215. https://doi.org/10.1002/2013JG002597.

Frankenberg, C., Fisher, J.B., Worden, J., Badgley, G., Saatchi, S.S., Lee, J.E., et al., 2011. New global observations of the terrestrial carbon cycle from GOSAT: patterns of plant fluorescence with gross primary productivity. Geophys. Res. Lett. 38, 351–365. https://doi.org/10.1029/2011GL048738.

Frankenberg, C., O'Dell, C., Berry, J., Guanter, L., Joiner, J., Koehler, P., et al., 2014. Prospects for chlorophyll fluorescence remote sensing from the orbiting carbon Observatory-2. Remote Sens. Environ. 147, 1–12. https://doi.org/10.1016/j.rse.2014.02.007.

Galvagno, M., Wohlfahrt, G., Cremonese, E., Rossini, M., Colombo, R., Filippa, G., et al., 2013. Phenology and carbon dioxide source/sink strength of a subalpine grassland in response to an exceptionally short snow season. Environ. Res. Lett. 8, 025008 https://doi.org/10.1088/1748-9326/8/2/025008.

Gao, Y., Wang, S., Guan, K., Wolanin, A., You, L., Ju, W., Zhang, Y., 2020. The ability of sun-induced chlorophyll fluorescence from OCO-2 and MODIS-EVI to monitor spatial variations of soybean and maize yields in the midwestern USA. Remote Sens. 12, 1111. https://doi.org/10.3390/rs12071111.

Gensheimer, J., Turner, A.J., Köhler, P., Frankenberg, C., Chen, J., 2022. A convolutional neural network for spatial downscaling of satellite-based solar-induced chlorophyll fluorescence (SIFnet). Biogeosciences 19, 1777–1793. https://doi.org/10.5194/bg-19-1777-2022.

Gentine, P., Alemohammad, S., 2018. Reconstructed solar induced fluorescence: a machine-learning vegetation product based on MODIS surface reflectance to reproduce GOME-2 solar induced fluorescence. Geophys. Res. Lett. 45, 3136–3146. https://doi.org/10.1002/2017GL076294.

Gobron, N., Morgan, O., Adams, J., Brown, L.A., Cappucci, F., Dash, J., et al., 2022. Evaluation of sentinel-3A and sentinel-3B ocean land colour instrument green instantaneous fraction of absorbed photosynthetically active radiation. Remote Sens. Environ. 270 https://doi.org/10.1016/j.rse.2021.112850.

Gruenwald, T., Bernhofer, C., 2007. A decade of carbon, water and energy flux measurements of an old spruce forest at the Anchor Station Tharandt. Tellus B 59, 387–396. https://doi.org/10.1111/j.1600-0889.2007.00259.x.

Guan, K., Berry, J.A., Zhang, Y., Joiner, J., Guanter, L., Badgley, G., Lobell, D.B., 2016. Improving the monitoring of crop productivity using spaceborne solar-induced fluorescence. Glob. Chang. Biol. 22, 716–726. https://doi.org/10.1111/gcb.13136.

Guanter, L., Bacour, C., Schneider, A., Aben, I., van Kempen, T.A., Maignan, F., et al., 2021. The TROPOSIF global sun-induced fluorescence dataset from the sentinel-5P TROPOMI mission. Earth Syst. Sci. Data 13, 5423–5440. https://doi.org/10.5194/essd-13-5423-2021.

Guanter, L., Frankenberg, C., Dudhia, A., Lewis, P.E., Gómez-Dans, J., Kuze, A., et al., 2012. Retrieval and global assessment of terrestrial chlorophyll fluorescence from GOSAT space measurements. Remote Sens. Environ. 121, 236–251. https://doi.org/10.1016/j.rse.2012.02.006.

Guanter, L., Zhang, Y., Jung, M., Joiner, J., Voigt, M., Berry, J.A., 2014. Global and time-resolved monitoring of crop photosynthesis with chlorophyll fluorescence. Proc. Natl. Acad. Sci. USA 111, E1327–E1333. https://doi.org/10.1073/pnas.1320008111.

He, L., Chen, J.M., Pisek, J., Schaaf, C.B., Strahler, A.H., 2012. Global clumping index map derived from the MODIS BRDF product. Remote Sens. Environ. 119, 118–130. https://doi.org/10.1016/j.rse.2011.12.008.

Hoshika, Y., Fares, S., Savi, F., Gruening, C., Goded, I., De Marco, A., et al., 2017. Stomatal conductance models for ozone risk assessment at canopy level in two Mediterranean evergreen forests. Agric. For. Meteorol. 234–235, 212–221. https://doi.org/10.1016/j.agrformet.2017.01.005.

Hu, J., Jia, J., Ma, Y., Liu, L., Yu, H., 2022. A reconstructed global daily seamless SIF product at 0.05 degree resolution based on TROPOMI, MODIS and ERA5 data. Remote Sens. 14, 1504. https://doi.org/10.3390/rs14061504.

Hussain, M.Z., Grünwald, T., Tenhunen, J.D., Li, Y.L., Mirzae, H., Bernhofer, C., et al., 2011. Summer drought influence on CO2 and water fluxes of extensively managed grassland in Germany. Agric. Ecosyst. Environ. 141, 67–76. https://doi.org/10.1016/j.agee.2011.02.013.

Hutley, L.B., Beringer, J., Isaac, P.R., Hacker, J.M., Cernusak, L.A., 2011. A sub-continental scale living laboratory: spatial patterns of savanna vegetation over a rainfall gradient in northern Australia. Agric. For. Meteorol. 151, 1417–1428. https://doi.org/10.1016/j.agrformet.2011.03.002.

Ilvesniemi, H., LevuIa, J., Ojansuu, R., KoIari, P., KuImaIa, L., Pumpanen, J., et al., 2009. Long-term measurements of the carbon balance of a boreal scots pine dominated forest ecosystem. Boreal Environ. Res. 14, 731–753. https://doi.org/10.1016/j.agrformet.2011.01.006.

Imer, D., Merbold, L., Eugster, W., Buchmann, N., 2013. Temporal and spatial variations of soil CO2, CH4 and N2O fluxes at three differently managed grasslands. Biogeosciences 10, 5931–5945. https://doi.org/10.5194/bg-10-5931-2013.

Irvine, J., Law, B.E., Martin, J.G., Vickers, D., 2008. Interannual variation in soil CO2 efflux and the response of root respiration to climate and canopy gas exchange in mature ponderosa pine. Glob. Chang. Biol. 14, 2848–2859. https://doi.org/10.1111/j.1365-2486.2008.01682.x.

Janssens, I.A., Kowalski, A.S., Ceulemans, R., 2001. Forest floor CO2 fluxes estimated by eddy covariance and chamber-based model. Agric. For. Meteorol. 106, 61–69. https://doi.org/10.1016/S0168-1923(00)00177-5.

Joiner, J., Yoshida, Y., Vasilkov, A.P., Yoshida, Y., Corp, L.A., Middleton, E.M., 2011. First observations of global and seasonal terrestrial chlorophyll fluorescence from space. Biogeosciences 8, 637–651. https://doi.org/10.5194/bg-8-637-2011.

Knohl, A., Schulze, E.-D., Kolle, O., Buchmann, N., 2003. Large carbon uptake by an unmanaged 250-year-old deciduous forest in Central Germany. Agric. For. Meteorol. 118, 151–167. https://doi.org/10.1016/S0168-1923(03)00115-1.

Knyazikhin, Y., Schull, M.A., Stenberg, P., Mottus, M., Rautiainen, M., Yang, Y., 2013. Hyperspectral remote sensing of foliar nitrogen content. Proc. Natl. Acad. Sci. USA 110, E185–E192. https://doi.org/10.1073/pnas.1210196109.

Köhler, P., Behrenfeld, M.J., Landgraf, J., Joiner, J., Magney, T.S., Frankenberg, C., 2020. Global retrievals of solar-induced chlorophyll fluorescence at red wavelengths with TROPOMI. Geophys. Res. Lett. 47, e2020GL087541 https://doi.org/10.1029/2020GL087541.

Köhler, P., Frankenberg, C., Magney, T.S., Guanter, L., Joiner, J., Landgraf, J., 2018. Global retrievals of solar-induced chlorophyll fluorescence with TROPOMI: first results and intersensor comparison to OCO-2. Geophys. Res. Lett. 45, 10456–10463. https://doi.org/10.5194/bg-12-4067-2015.

Kong, J., Ryu, Y., Liu, J., Dechant, B., Rey-Sanchez, C., Shortt, R., et al., 2022. Matching high resolution satellite data and flux tower footprints improves their agreement in photosynthesis estimates. Agric. For. Meteorol. 316, 108878 https://doi.org/10.1016/j.agrformet.2022.108878.

Kurbatova, J., Li, C., Varlagin, A., Xiao, X., Vygodskaya, N., 2008. Modeling carbon dynamics in two adjacent spruce forests with different soil conditions in Russia. Biogeosciences 5, 969–980. https://doi.org/10.5194/bg-5-969-2008.

Leuning, R., Cleugh, H.A., Zegelin, S.J., Hughes, D., 2005. Carbon and water fluxes over a temperate eucalyptus forest and a tropical wet/dry savanna in Australia: measurements and comparison with MODIS remote sensing estimates. Agric. For. Meteorol. 129, 151–173. https://doi.org/10.1016/j.agrformet.2004.12.004.
Li, X., Xiao, J., 2019a. A global, 0.05-degree product of solar-induced chlorophyll fluorescence derived from OCO-2, MODIS, and reanalysis data. Remote Sens. 11, 517. https://doi.org/10.3390/rs11050517.
Li, X., Xiao, J., He, B., Arain, M.A., Beringer, J., Desai, A.R., et al., 2018. Solar-induced chlorophyll fluorescence is strongly correlated with terrestrial photosynthesis for a wide variety of biomes: first global analysis based on OCO-2 and flux tower observations. Glob. Chang. Biol. 24, 3990–4008. https://doi.org/10.1111/gcb.14297.
Li, X., Xiao, J.F., 2019b. Mapping photosynthesis solely from solar-induced chlorophyll fluorescence: a global, fine-resolution dataset of gross primary production derived from OCO-2. Remote Sens. 11, 2563. https://doi.org/10.3390/rs11212563.
Liang, S., 2001. Narrowband to broadband conversions of land surface albedo I: algorithms. Remote Sens. Environ. 76, 213–238. https://doi.org/10.1016/S0034-4257(00)00205-4.
Liu, X., Guanter, L., Liu, L., Damm, A., Malenovský, Z., Rascher, U., et al., 2019. Downscaling of solar-induced chlorophyll fluorescence from canopy level to photosystem level using a random forest model. Remote Sens. Environ. 231, 110772 https://doi.org/10.1016/j.rse.2018.05.035.
Liu, X., Liu, L., Hu, J., Guo, J., Du, S., 2020. Improving the potential of red SIF for estimating GPP by downscaling from the canopy level to the photosystem level. Agric. For. Meteorol. 281, 107846 https://doi.org/10.1016/j.agrformet.2019.107846.
Liu, Y., Chen, J.M., He, L., Zhang, Z., Wang, R., Rogers, C., et al., 2022. Non-linearity between gross primary productivity and far-red solar-induced chlorophyll fluorescence emitted from canopies of major biomes. Remote Sens. Environ. 271, 112896 https://doi.org/10.1016/j.rse.2022.112896.
Lu, X., Liu, Z., Zhao, F., Tang, J., 2020. Comparison of total emitted solar-induced chlorophyll fluorescence (SIF) and top-of-canopy (TOC) SIF in estimating photosynthesis. Remote Sens. Environ. 251, 112083 https://doi.org/10.1016/j.rse.2020.112083.
Lucht, W., Schaaf, C.B., Strahler, A.H., 2000. An algorithm for the retrieval of albedo from space using semiempirical BRDF models. IEEE Trans. Geosci. Remote Sens. 38, 977–998. https://doi.org/10.1109/36.841980.
Luo, Y., El-Madany, T.S., Filippa, G., Ma, X., Ahrens, B., Carrara, A., et al., 2018. Using near-infrared-enabled digital repeat photography to track structural and physiological phenology in Mediterranean tree–grass ecosystems. Remote Sens. 10, 1293. https://doi.org/10.3390/rs10081293.
Lyapustin, A., Wang, Y., Korkin, S., Huang, D., 2018. MODIS collection 6 MAIAC algorithm. Atmos. Meas. Tech. 11, 5741–5765. https://doi.org/10.5194/amt-11-5741-2018.
Ma, S.Y., Baldocchi, D.D., Xu, L.K., Hehn, T., 2007. Inter-annual variability in carbon dioxide exchange of an oak/grass savanna and open grassland in California. Agric. For. Meteorol. 147, 157–171. https://doi.org/10.1016/j.agrformet.2007.07.008.
Ma, Y., Liu, L., Liu, X., Chen, J., 2022. An improved downscaled sun-induced chlorophyll fluorescence (DSIF) product of GOME-2 dataset. Eur. J. Remote Sens. 55, 168–180. https://doi.org/10.1080/22797254.2022.2028579.
Magney, T.S., Barnes, M.L., Yang, X., 2020. On the covariation of chlorophyll fluorescence and photosynthesis across scales. Geophys. Res. Lett. 47, e2020GL091098 https://doi.org/10.1029/2020GL091098.
Meyer, W., Kondrlovà, E., Koerber, G., 2015. Evaporation of perennial semi-arid woodland in southeastern Australia is adapted for irregular but common dry periods. Hydrol. Process. 29, 3714–3726. https://doi.org/10.1002/hyp.10467.
Milyukova, I.M., Kolle, O., Varlagin, A.V., Vygodskaya, N.N., Schulze, E.D., Lloyd, J., 2002. Carbon balance of a southern taiga spruce stand in european Russia. Tellus B 54, 429–442. https://doi.org/10.3402/tellusb.v54i5.16679.
Missik, J.E.C., Liu, H., Gao, Z., Huang, M., Chen, X., Arntzen, E., et al., 2019. Groundwater-River water exchange enhances growing season evapotranspiration and carbon uptake in a semiarid riparian ecosystem. J. Geophys. Res. Biogeosci. 124, 99–114. https://doi.org/10.1029/2018JG004666.
Monson, R., Turnipseed, A., Sparks, J., Harley, P., Scott-Denton, L., Sparks, K., Huxman, T., 2002. Carbon sequestration in a high-elevation, subalpine forest. Glob. Chang. Biol. 8, 459–478. https://doi.org/10.1046/j.1365-2486.2002.00480.x.
Moureaux, C., Debacq, A., Bodson, B., Heinesch, B., Aubinet, M., 2006. Annual net ecosystem carbon exchange by a sugar beet crop. Agric. For. Meteorol. 139, 25–39. https://doi.org/10.1016/j.agrformet.2006.05.009.
Myneni, R., Knyazikhin, Y., Park, T., 2015. MCD15A2H MODIS/Terra+ aqua leaf area Index/FPAR 8-day L4 global 500 m SIN grid V006. Distrib. NASA EOSDIS Land Process. DAAC. https://doi.org/10.5067/MODIS/MCD15A2H.006.
Myneni, R.B., Hoffman, S., Knyazikhin, Y., Privette, J.L., Glassy, J., Tian, Y., et al., 2002. Global products of vegetation leaf area and fraction absorbed PAR from year one of MODIS data. Remote Sens. Environ. 83, 214–231. https://doi.org/10.1016/S0034-4257(02)00074-3.
Peng, B., Guan, K., Zhou, W., Jiang, C., Frankenberg, C., Sun, Y., et al., 2020. Assessing the benefit of satellite-based solar-induced chlorophyll fluorescence in crop yield prediction. Int. J. Appl. Earth Obs. Geoinf. 90, 102126 https://doi.org/10.1016/j.jag.2020.102126.
Pierini, N.A., Vivoni, E.R., Robles-Morua, A., Scott, R.L., Nearing, M.A., 2014. Using observations and a distributed hydrologic model to explore runoff thresholds linked with mesquite encroachment in the Sonoran Desert. Water Resour. Res. 50, 8191–8215. https://doi.org/10.1002/2014WR015781.
Pilegaard, K., Ibrom, A., 2020. Net carbon ecosystem exchange during 24 years in the Sorø beech Forest – relations to phenology and climate. Tellus B 72, 1–17. https://doi.org/10.1080/16000889.2020.1822063.
Porcar-Castell, A., Malenovský, Z., Magney, T., Van Wittenberghe, S., Fernández-Marín, B., Maignan, F., et al., 2021. Chlorophyll a fluorescence illuminates a path connecting plant molecular biology to earth-system science. Nat. Plants 7, 998–1009. https://doi.org/10.1038/s41477-021-00980-4.
Post, H., Hendricks Franssen, H.-J., Graf, A., Schmidt, M., Vereecken, H., 2015. Uncertainty analysis of eddy covariance CO2 flux measurements for different EC tower distances using an extended two-tower approach. Biogeosciences 12, 1205–1221. https://doi.org/10.5194/bg-12-1205-2015.
Prober, S.M., Thiele, K.R., Rundel, P.W., Yates, C.J., Berry, S.L., Byrne, M., et al., 2012. Facilitating adaptation of biodiversity to climate change: a conceptual framework applied to the world's largest Mediterranean-climate woodland. Clim. Chang. 110, 227–248. https://doi.org/10.1007/s10584-011-0092-y.
Qiu, R., Han, G., Ma, X., Sha, Z., Shi, T., Xu, H., Zhang, M., 2020. CO2 concentration, a critical factor influencing the relationship between solar-induced chlorophyll fluorescence and gross primary productivity. Remote Sens. 12, 1377. https://doi.org/10.3390/rs12091377.
Rambal, S., Joffre, R., Ourcival, J., Cavender-Bares, J., Rocheteau, A., 2004. The growth respiration component in eddy CO2 flux from a Quercus ilex mediterranean forest. Glob. Chang. Biol. 10, 1460–1469. https://doi.org/10.1111/j.1365-2486.2004.00819.x.
Reichstein, M., Falge, E., Baldocchi, D., Papale, D., Aubinet, M., Berbigier, P., et al., 2005. On the separation of net ecosystem exchange into assimilation and ecosystem respiration: review and improved algorithm. Glob. Chang. Biol. 11, 1424–1439. https://doi.org/10.1111/j.1365-2486.2005.001002.x.
Ruehr, N.K., Martin, J.G., Law, B.E., 2012. Effects of water availability on carbon and water exchange in a young ponderosa pine forest: above- and belowground responses. Agric. For. Meteorol. 164, 136–148. https://doi.org/10.1016/j.agrformet.2006.05.009.
Ryu, Y., Jiang, C., Kobayashi, H., Detto, M., 2018. MODIS-derived global land products of shortwave radiation and diffuse and total photosynthetically active radiation at 5 km resolution from 2000. Remote Sens. Environ. 204, 812–825. https://doi.org/10.1016/j.rse.2017.09.021.
Scott, R.L., Biederman, J.A., Hamerlynck, E.P., Barron-Gafford, G.A., 2015. The carbon balance pivot point of southwestern U.S. Semiarid ecosystems: insights from the 21st century drought. J. Geophys. Res. Biogeosci. 120, 2612–2624. https://doi.org/10.1002/2015JG003181.
Scott, R.L., Hamerlynck, E.P., Jenerette, G.D., Moran, M.S., Barron-Gafford, G.A., 2010. Carbon dioxide exchange in a semidesert grassland through drought-induced vegetation change. J. Geophys. Res. Biogeosci. 115, G03026. https://doi.org/10.1029/2010JG001348.
Scott, R.L., Jenerette, G.D., Potts, D.L., Huxman, T.E., 2009. Effects of seasonal drought on net carbon dioxide exchange from a woody-plant-encroached semiarid grassland. J. Geophys. Res. Biogeosci. 114, G04004. https://doi.org/10.1029/2008JG000900.
Sloat, L.L., Lin, M., Butler, E.E., Johnson, D., Holbrook, N.M., Huybers, P.J., et al., 2021. Evaluating the benefits of chlorophyll fluorescence for in-season crop productivity forecasting. Remote Sens. Environ. 260, 112478 https://doi.org/10.1016/j.rse.2021.112478.
Sulman, B., Desai, A., Cook, B., Saliendra, N., Mackay, D., 2009. Contrasting carbon dioxide fluxes between a drying shrub wetland in northern Wisconsin, USA, and nearby forests. Biogeosciences 6, 1115–1126. https://doi.org/10.5194/bg-6-1115-2009.
Sun, Y., Frankenberg, C., Jung, M., Joiner, J., Guanter, L., Köhler, P., Magney, T., 2018. Overview of solar-induced chlorophyll fluorescence (SIF) from the orbiting carbon Observatory-2: retrieval, cross-mission comparison, and global monitoring for GPP. Remote Sens. Environ. 209, 808–823. https://doi.org/10.1016/j.rse.2018.02.016.
Sun, Y., Frankenberg, C., Wood, J.D., Schimel, D.S., Jung, M., Guanter, L., et al., 2017. OCO-2 advances photosynthesis observation from space via solar-induced chlorophyll fluorescence. Science 358, eaam5747. https://doi.org/10.1126/science.aam5747.
Taylor, T.E., Eldering, A., Merrelli, A., Kiel, M., Somkuti, P., Cheng, C., et al., 2020. OCO-3 early mission operations and initial (vEarly) XCO2 and SIF retrievals. Remote Sens. Environ. 251, 112032 https://doi.org/10.1016/j.rse.2020.112032.
Ueyama, M., Iwata, H., Harazono, Y., 2014. Autumn warming reduces the CO2 sink of a black spruce forest in interior Alaska based on a nine-year eddy covariance measurement. Glob. Chang. Biol. 20, 1161–1173. https://doi.org/10.1111/gcb.12434.
Urbanski, S., Barford, C., Wofsy, S., Kucharik, C., Pyle, E., Budney, J., et al., 2007. Factors controlling CO2 exchange on timescales from hourly to decadal at Harvard Forest. J. Geophys. Res. Biogeosci. 112, G02020. https://doi.org/10.1029/2006jg000293.
Verma, M., Schimel, D., Evans, B., Frankenberg, C., Beringer, J., Drewry, D.T., et al., 2017. Effect of environmental conditions on the relationship between solar-induced fluorescence and gross primary productivity at an OzFlux grassland site. J. Geophys. Res. Biogeosci. 122, 716–733. https://doi.org/10.1002/2016JG003580.
Wang, S., Zhang, Y., Ju, W., Porcar-Castell, A., Ye, S., Zhang, Z., et al., 2020a. Warmer spring alleviated the impacts of 2018 european summer heatwave and drought on vegetation photosynthesis. Agric. For. Meteorol. 295, 108195 https://doi.org/10.1016/j.agrformet.2020.108195.
Wang, X., Chen, J.M., Ju, W., 2020b. Photochemical reflectance index (PRI) can be used to improve the relationship between gross primary productivity (GPP) and sun-induced chlorophyll fluorescence (SIF). Remote Sens. Environ. 246, 111888 https://doi.org/10.1016/j.rse.2020.111888.
Wen, J., Köhler, P., Duveiller, G., Parazoo, N.C., Magney, T.S., Hooker, G., et al., 2020. A framework for harmonizing multiple satellite instruments to generate a long-term

global high spatial-resolution solar-induced chlorophyll fluorescence (SIF). Remote Sens. Environ. 239, 111644 https://doi.org/10.1016/j.rse.2020.111644.

Wood, J.D., Griffis, T.J., Baker, J.M., Frankenberg, C., Verma, M., Yuen, K., 2017. Multiscale analyses of solar-induced florescence and gross primary production. Geophys. Res. Lett. 44, 533–541. https://doi.org/10.1002/2016gl070775.

Yang, P., van der Tol, C., 2018. Linking canopy scattering of far-red sun-induced chlorophyll fluorescence with reflectance. Remote Sens. Environ. 209, 456–467. https://doi.org/10.1016/j.rse.2018.02.029.

Yang, P., van der Tol, C., Campbell, P.K.E., Middleton, E.M., 2020. Fluorescence correction vegetation index (FCVI): a physically based reflectance index to separate physiological and non-physiological information in far-red sun-induced chlorophyll fluorescence. Remote Sens. Environ. 240, 111676 https://doi.org/10.1016/j.rse.2020.111676.

Yee, M.S., Pauwels, V.R., Daly, E., Beringer, J., Rüdiger, C., McCabe, M.F., Walker, J.P., 2015. A comparison of optical and microwave scintillometers with eddy covariance derived surface heat fluxes. Agric. For. Meteorol. 213, 226–239. https://doi.org/10.1016/j.agrformet.2015.07.004.

Yu, L., Wen, J., Chang, C.Y., Frankenberg, C., Sun, Y., 2019. High-resolution global contiguous SIF of OCO-2. Geophys. Res. Lett. 46, 1449–1458. https://doi.org/10.1029/2018gl081109.

Zeng, Y., Badgley, G., Dechant, B., Ryu, Y., Chen, M., Berry, J., 2019. A practical approach for estimating the escape ratio of near-infrared solar-induced chlorophyll fluorescence. Remote Sens. Environ. 232, 211209 https://doi.org/10.1016/j.rse.2019.05.028.

Zhang, Y., Joiner, J., Alemohammad, S.H., Zhou, S., Gentine, P., 2018a. A global spatially contiguous solar-induced fluorescence (CSIF) dataset using neural networks. Biogeosciences 15, 5779–5800. https://doi.org/10.5194/bg-15-5779-2018.

Zhang, Z., Zhang, Y., 2023. Solar angle matters: diurnal pattern of solar-induced chlorophyll fluorescence from OCO-3 and TROPOMI. Remote Sens. Environ. 285, 113380 https://doi.org/10.1016/j.rse.2022.113380.

Zhang, Z.Y., Chen, J.M., Guanter, L., He, L.M., Zhang, Y.G., 2019. From canopy-leaving to total canopy far-red fluorescence emission for remote sensing of photosynthesis: first results from TROPOMI. Geophys. Res. Lett. 46, 12030–12040. https://doi.org/10.1029/2019GL084832.

Zhang, Z.Y., Zhang, Y., Chen, J.M., Ju, W., Migliavacca, M., El-Madany, T.S., 2021. Sensitivity of estimated total canopy SIF emission to remotely sensed LAI and BRDF products. J. Remote Sens. 2021, 9795837. https://doi.org/10.34133/2021/9795837.

Zhang, Z.Y., Zhang, Y.G., Joiner, J., Migliavacca, M., 2018b. Angle matters: bidirectional effects impact the slope of relationship between gross primary productivity and sun-induced chlorophyll fluorescence from orbiting carbon Observatory-2 across biomes. Glob. Chang. Biol. 24, 5017–5020. https://doi.org/10.1111/gcb.14427.

Zhang, Z.Y., Zhang, Y.G., Porcar-Castell, A., Joiner, J., Guanter, L., Yang, X., et al., 2020a. Reduction of structural impacts and distinction of photosynthetic pathways in a global estimation of GPP from space-borne solar-induced chlorophyll fluorescence. Remote Sens. Environ. 240, 111722 https://doi.org/10.1016/j.rse.2020.111722.

Zhang, Z.Y., Zhang, Y.G., Zhang, Q., Chen, J.M., Porcar-Castell, A., Guanter, L., et al., 2020b. Assessing bi-directional effects on the diurnal cycle of measured solar-induced chlorophyll fluorescence in crop canopies. Agric. For. Meteorol. 295, 108147 https://doi.org/10.1016/j.agrformet.2020.108147.

Zhang, Z.Y., Zhang, Y.G., Zhang, Y., Chen, J.M., 2020c. Correcting clear-sky bias in gross primary production modeling from satellite solar-induced chlorophyll fluorescence data. Journal of geophysical research. Biogeosciences 125, e2020JG005822. https://doi.org/10.1029/2020jg005822.

Zhang, Z.Y., Zhang, Y.G., Zhang, Y., Gobron, N., Frankenberg, C., Wang, S., Li, Z., 2020d. The potential of satellite FPAR product for GPP estimation: an indirect evaluation using solar-induced chlorophyll fluorescence. Remote Sens. Environ. 240, 111686 https://doi.org/10.1016/j.rse.2020.111686.

Zielis, S., Etzold, S., Zweifel, R., Eugster, W., Haeni, M., Buchmann, N., 2014. NEP of a swiss subalpine forest is significantly driven not only by current but also by previous year's weather. Biogeosciences 11, 1627–1635. https://doi.org/10.5194/bg-11-1627-2014.